Mining, Metallurgy & Exploration (2022) 39:1939–1960
https://doi.org/10.1007/s42461-022-00664-3

Analysis of SLAM-Based Lidar Data Quality Metrics for Geotechnical Underground Monitoring

Lukas Fahle[1] · Elizabeth A. Holley[1] · Gabriel Walton[1] · Andrew J. Petruska[1] · Jurgen F. Brune[1]

Received: 4 November 2021 / Accepted: 28 July 2022 / Published online: 16 August 2022

Abstract
Adverse ground behavior events, such as convergence and ground falls, pose critical risks to underground mine safety and productivity. Today, monitoring of such failures is primarily conducted using legacy techniques with low spatial and temporal resolution while exposing workers to hazardous environments. This study assesses the potential of novel simultaneous localization and mapping (SLAM)-based light detection and ranging (Lidar) data quality for rapid, digital, and eventually autonomous mine-wide underground geotechnical monitoring. We derive a comprehensive suite of quality metrics based on tests in two underground mines for two state-of-the-art mobile laser scanning (MLS) systems. Our results provide evidence that SLAM-based MLS provides data of the quality required to detect geotechnically relevant changes while being significantly more efficient for large mine layouts when compared to traditional static systems. Additionally, we show that SLAM-specific processing can achieve an order of magnitude better relative accuracy relevant for change detection than quality metrics derived from traditionally deployed tests would suggest while reducing SLAM drift error by up to 90%. In collaboration with an operating block cave mine, we confirm these capabilities in field tests on a mine-wide scale and, for the first time, demonstrate methods of rockfall detection using MLS data. While more work is required to investigate optimal collection, processing, and utilization of MLS data, we demonstrate its potential to become an effective and widely applicable data source for rapid, accurate, and comprehensive geotechnical inspections.

Keywords Mobile laser scanning · Simultaneous Localization and Mapping (SLAM) · Geotechnical monitoring · Change detection · Rockfall and convergence

1 Introduction

Adverse ground behavior events, such as convergence and rock and ground falls, pose some of the most significant risks in underground mines. Fall of ground events, i.e., the dislodging and fall of rock or shotcrete from mine drift faces, ribs, and roofs, are hazards to personnel and non-human assets in US and international underground coal, metal, and nonmetal mines [1–6]. Therefore, geotechnical monitoring and ground control ensure the safety of underground mines, operational reliability, and economic viability. The need for near real-time and mine-wide geotechnical situational awareness will become more prominent with the increasing depth of mines, more challenging ground conditions, and fewer personnel at the face [7, 8].

Many surface mining operations utilize automated remote sensing tools such as radar and robotic total stations for efficient mine-wide, real-time geotechnical monitoring [9, 10]. In contrast, underground mines primarily rely on in-person, visual inspections and stationary sensors with a limited spatial resolution [11]. Visual inspections generate analog, qualitative, and low-accuracy data of variable accuracy and cannot deliver technically robust data on a frequent, mine-wide scale. In contrast, embedded sensors

Highlights
- Mobile laser scanning data quality at or above the required accuracy for geotechnical monitoring can be achieved.
- Sub-millimeter relative trueness and millimeter relative precision can be achieved in multi-epoch comparisons.
- SLAM-based lidar data acquisition is significantly more efficient than static lidar when applied over large mine areas.
- SLAM-based loop closure decreases drift error by up to 90% and improves intrinsic SLAM precision.
- SLAM-based scan registration outperforms traditional methods and eliminates site-level drift error.

✉ Lukas Fahle
lukasfahle@mines.edu

[1] Colorado School of Mines, Golden, CO, USA

such as multi-point borehole extensometers can provide high accuracy, 2D digital data at a much higher temporal resolution. However, their spatial resolution as a function of the number of deployed sensors is limited by installation and maintenance costs. Stationary remote sensors, such as tripod-mounted light detection and ranging (Lidar) scanners, have been used to collect high-accuracy three-dimensional data for several underground applications, including geotechnical monitoring [12]. Besides limitations in terms of accuracy, spatial, and temporal resolution, traditional monitoring techniques also expose personnel to some of the most common hazards in underground mining—slips, trips, and falls, ground fall, and vehicle impact [13].

Our work investigates novel simultaneous localization and mapping (SLAM) mobile Lidar scanning (MLS) to enable frequent, mine-wide geotechnical monitoring. In contrast to static lidar scanners, an MLS system can be locomoted during data collection, significantly reducing the data acquisition time compared to static lidar and other traditional monitoring methods. While uncrewed aerial vehicle (UAV) lidar scanning is now standard for areas with limited access, such as stopes [14], mine-wide mapping, change detection, and monitoring are still in their early stages. Therefore, many questions related to underground SLAM-based MLS monitoring that are highly relevant to users (e.g., geotechnical engineers, mine management) and suppliers (instrumentation, equipment, and software developers and manufacturers) are currently unanswered.

The primary contribution of this paper is an in-depth and geotechnically focused investigation of multiple state-of-the-art SLAM MLS systems in multiple underground mines. For the first time, we show that MLS data can be utilized for rapid, mine-wide detection of convergence and is capable of detecting centimeter-scale discrete geotechnical failures such as rockfall. We also demonstrate significantly higher relative accuracy than traditional absolute accuracy metrics suggest for multi-epoch underground mine MLS data. We achieve this with SLAM-based loop closure to minimize drift error by up to 90% and SLAM-based scan registration. Our results provide evidence that SLAM-based MLS can deliver data quality at or above the required accuracy for geotechnical monitoring while being significantly faster than static LiDAR or other traditional monitoring methods.

2 Review of Lidar for Geotechnical Applications

2.1 The Need for Underground Geotechnical Monitoring

In underground mining and tunneling, rock mass deformation or convergence manifests in cross section area changes and results from the redistribution of in situ stresses around an excavation [15]. An acceleration of strain can indicate an onset of tertiary creep, which in brittle rock will be accompanied by fracturing, rock block releases, and eventually collapse of the excavation [16]. While convergence is often observed over relatively large spatial extents, more discrete rock block or slab releases in the roof (roof fall) or the rib (rib spalling) can be an associated failure and act as both precursors and symptoms of convergence. Although the magnitudes and rates of these geotechnical failures depend on various factors (e.g., rockmass conditions, magnitude, orientation, and the ratio of the in situ stresses, extraction methods and rate and type and location of installed support), absolute strain and strain rates can differ significantly from mine to mine [17]. Critical magnitudes with a potential negative impact on safety and productivity can be classified by diametrical stain anywhere from 1 to 10%, i.e., 0.05 to 0.5 m of wall-to-wall convergence in a 5-m-wide drift [18]. Such steady-state convergence rates will eventually require rehabilitation work or redesigns, potentially creating mid- to long-term operational challenges. Associated rockfall events are a more imminent threat to mine personnel and equipment. Rockfalls as small as 10 cm in diameter have been shown to cause fatal injuries in underground mines [19], but are often hard to detect and monitor on a mine-wide scale. For mine-wide monitoring of geotechnical hazards, we can assume that a practical limit of detection for convergence should at most be 0.05 m wall-to-wall change and 0.1 m of change for evaluating rockfall events.

2.2 Mobile Lidar Scanning in Underground Geotechnical Monitoring

Numerous studies have examined the use of static lidar for characterization and multi-epoch monitoring of failures common for surface mine and rock slope engineering applications. Static lidar is primarily used to monitor relatively small regions of interest with known geotechnical hazards such as rockfall [20–33]. In underground excavations, static LiDAR has been primarily deployed for single-epoch mapping of geological features and properties such as structural discontinuities and surface characteristics [34, 35]. Static lidar has also been investigated for multi-epoch monitoring of geotechnical deformations and changes in underground construction and tunneling [12, 17, 36–45]. So far, most of these studies have focused on monitoring progressive changes such as displacements caused by convergence. Only a few authors have investigated discrete failure types such as rockfall, roof sag, or spalling of shotcrete [36, 46, 47]. The main obstacle to the widespread adoption of static lidar-based underground monitoring is the slow data collection speed that makes frequent (e.g., daily or weekly) monitoring campaigns of large areas impractical.

SLAM-based MLS shows promise for large-scale, multi-epoch, and frequent underground mine monitoring applications. Since mobile units, such as standalone MLS and sensor payloads on autonomous mining equipment, do not need to be set up at a specific scan station, they can significantly increase lidar data collection speed. MLS data's high temporal and spatial resolution makes it ideal for rock mass deformation and failure monitoring applications [16, 18]. Although research on mobile lidar systems in underground environments has been ongoing for more than 20 years, geotechnical monitoring of the failures described above has not been investigated in much detail (Table 1).

Heavy mining equipment automation research introduced the concept of mobile laser scanning in underground mines [46]. Parallel research efforts concentrated on the robotic exploration of non-operating mines with purpose-built robotic platforms [49]. Subsequent improvements in simultaneous localization and mapping (SLAM) techniques were then leveraged to develop MLS that were used to produce 2D and 3D maps of mines and caves [50, 51]. Zlot and Bosse's [50, 52] work and other studies using MLS developed by GeoSLAM (e.g., [53–57]) comprised some of the first systematic studies that tested the accuracy of MLS in indoor and outdoor environments, including underground mines. The results of the prior studies indicate that point clouds generated with the tested MLS can achieve a target-level accuracy of 1–3 cm, but SLAM drift error and noise can significantly increase errors at a site-wide scale. Multi-temporal and mine-wide scanning for change detection have not previously been investigated in much detail.

Lavigne and Marshall [58] described a different approach in tackling the SLAM problem for underground mine mapping by localizing an MLS against local metric sub-maps tied to RFID tags to reduce the drift error in large-scale and unknown environments. To perform monitoring of convergence, Lynch et al. [59] and Vanderbeck [60] later used data from a commercial MLS based on the system developed by Lavigne and Marshall [58]. Significant drift and scan alignment errors were encountered in field tests in underground mines, and no conclusive results regarding the performance of the convergence detection based on field data were presented [61].

Data quality limitations of earlier mobile lidar systems have rendered them mostly impractical for large-scale, frequent geotechnical monitoring applications in operating mines. Improvements in the quality of compact lidar sensors and advancements in simultaneous localization and mapping (SLAM) algorithms recently led to the commercialization of the latest generation of compact SLAM-based MLS [86, 87]. These incorporate high-resolution lidar sensors and new SLAM algorithms optimized to improve target- and site-level data quality. New SLAM systems use loop closure to optimize trajectories and maps globally when the system recognizes a previously visited location [88, 89]. SLAM-based registration is another critical capability that allows new scan epochs to be registered to a baseline point cloud. The release of a new generation of compact MLS with advanced SLAM technology requires a closer investigation of MLS for mine-scale geotechnical monitoring.

3 Material and Methods

This study aims to provide a current and detailed analysis of MLS lidar data quality by deploying two state-of-the-art SLAM-based systems. We collected data in two underground mines: an operational block caving mine (Mine-A) and the Colorado School of Mines Edgar Experimental Mine (Edgar). We derived quality metrics on MLS data collection efficiency, density, coverage, and absolute and relative

Table 1 Research on mobile lidar data in underground environments

Domain	Lidar data use	Limitations	Literature
Equipment automation	Equipment perception and control	Low-resolution lidar No focus on mapping No multi-temporal comparison No focus on geotechnical monitoring	[48, 62–69]
Robotic exploration of abandoned mines	Robot perception and control Offline generation of rudimentary maps using simultaneous localization and mapping (SLAM) techniques	Low-resolution lidar Offline map generation No focus on geotechnical monitoring	[49, 70–79]
Cave and mine mapping	General and geological structure mapping	SLAM drift errors Noisy lidar data Limited to small-scale environments No focus on geotechnical monitoring	[50–55, 57, 80–85]
Geotechnical monitoring	Multi-epoch mapping and convergence monitoring	Drift errors without RFID infrastructure No conclusive results on convergence monitoring	[59–61]

accuracy metrics. Furthermore, we tested the effect of loop closure and SLAM-based registration on data accuracy. We also conducted specific geotechnical monitoring tests for rockfall and convergence detection. The study closes with a discussion of SLAM-based MLS data in underground geotechnical monitoring. Table 2 summarizes our experimental design, and the following sections detail our chosen accuracy metrics, instrumentation, data collection, processing, and analysis.

3.1 Accuracy Metrics

A key challenge in mine-scale MLS monitoring is the need for high data quality in spatiotemporally dynamic, large, and complex environments. On a spatial scale, achieving high local (target-level) and global (site-level) accuracy [90] is critical and depends on three types of errors [38]:

1. **Sensor-related:** range error, angular error, scanner noise, beam divergence and sport size, ambiguity interval (for phase-based lidar), scan density, and spatial resolution
2. **Environment-related**: surface reflectivity, angle of incidence, spurious scan points
3. **Processing-related:** georeferencing and alignment

In addition to target- and site-level accuracy, a differentiation between absolute and relative accuracy of MLS data is important. We define absolute accuracy as a measure of error between an MLS point cloud and a ground-truth representation of the scene, such as a surveyed static lidar point cloud. Relative accuracy measures the error between two MLS point clouds collected by the same system. The uniformity of data quality over space and time, measured, for example, in terms of density and coverage, is another critical quality metric for MLS-based monitoring [91] that we investigate. We also investigated intrinsic and extrinsic SLAM precision. Ideally, multiple instances of SLAM-based processing of one dataset with unchanged SLAM parameters should result in identical outputs. Any variation in the output can be attributed to intrinsic inaccuracies of the SLAM system and is part of the processing-related errors in lidar data. The extrinsic SLAM precision combines intrinsic SLAM inaccuracies with sensor and environment-associated errors. We determined intrinsic SLAM precision based on the distances of two SLAM outputs of the same scan. We measured extrinsic SLAM precision by comparing two independently collected scans of the same, unchanged scene and evaluated the differences between those scans.

Similar to Toschi et al. [92] we utilized parametric and non-parametric statistics to evaluate MLS data accuracy.

Table 2 Overview of tests, metrics, and instruments used in this study

Results section	Tested variable	Key metric	Spatial scale	Instrument	Site
Data quality investigation	Normality	Q-Q plot, skewness, kurtosis	Target- and site-level	Stencil 2/Hovermap	Mine-A/Edgar
	Density	Minimum spacing	Target- and site-level	Stencil 2/Hovermap/ Faro Focus S70	Mine-A
	Coverage	Percent occlusion	Target- and site-level	Stencil 2/Hovermap/ Faro Focus S70	Mine-A
	Absolute accuracy	Trueness (μ/m)	Target- and site-level	Stencil 2/Hovermap/ Faro Focus S70 and 3D X 330	Mine-A/Edgar
		Precision (σ/MAD)	Target- and site-level	Stencil 2/Hovermap/ Faro Focus S70 and 3D X 330	Mine-A/Edgar
	Relative accuracy	Trueness (μ/m)	Target level	Stencil 2/Hovermap	Mine-A/Edgar
		Precision (σ/MAD)	Target level	Stencil 2/Hovermap	Mine-A/Edgar
		Intrinsic and extrinsic SLAM precision (σ/MAD)	Site level	Hovermap	Edgar
MLS operational tests	Data collection efficiency	Points per second	Target- and site-level	Stencil 2/Hovermap/ Faro Focus S70	Mine-A
	Loop closure quality	Delta sensor accuracy and delta x, y, z static	Target- and site-level	Stencil 2/Hovermap/ Faro Focus 3D X 330	Edgar
	SLAM registration quality	m/MAD	Target- and site-level	Stencil 2/Faro Focus 3D X 330	Edgar
	Rockfall and convergence detection	Visual comparison/practical detection limit	Target- and site-level	Stencil 2/Hovermap	Mine-A/Edgar

μ, mean error of the distribution; m, median; σ, standard deviation; *MAD*, median absolute deviation

First, we determined if outlier robust (non-parametric) statistics must be utilized by testing if the data errors follow a normal (Gaussian) distribution. We tested the normality assumption using a graphical evaluation of Q-Q plots, skewness, and kurtosis measurers. The Q-Q plot allows for visual evaluation of normality for extensive sets of samples, i.e., the distances between point clouds. Normally distributed errors will plot as a straight line. Skewness provides an indication of departure from symmetry in a distribution and is expressed as:

$$\text{Skewness} = \frac{\sum_{i=1}^{n} \left(x_i - \mu\right)^3}{(n-1)\sigma^3}$$

where x_i is a random variable (i.e., the distance of a point i), μ the sample mean error of the distribution, n the number of variables in the distribution, and σ the standard deviation. Kurtosis is a measure of whether the data are peaked or flat relative to a normal distribution and is expressed as:

$$\text{Kurtosis} = \frac{\sum_{i=1}^{n} \left(x_i - \mu\right)^4}{(n-1)\sigma^4}$$

Normal distributions will display skewness values of 0 and kurtosis values of 3. We measure data accuracy as defined by the ISO [93] by its trueness, i.e., "the closeness of agreement between the arithmetic mean of a large number of test results and the true or accepted reference value," and precision, i.e., "the closeness of agreement between test results." The sample mean error μ and standard deviation σ can be utilized as metrics for trueness and precision if the normality hypothesis is supported. Non-Gaussian distributions can be evaluated using the median m for trueness and median absolute deviation MAD for precision. The MAD is defined as the median of the absolute deviations from the data's median (m_x)

$$\text{MAD} = m(|x_i - m_x|)$$

3.2 Instsrumentation

Both MLS systems used in this study are state-of-art in commercial mobile scanning and utilize a Velodyne Puck lidar sensor [94], inertial measurement unit (IMU), and their respective proprietary SLAM solutions. For comparison, we also collected static lidar data. At Mine-A, a static FARO Focus S70 LiDAR was operated by an experienced geotechnical engineer. At Edgar, we deployed a FARO Focus 3D X 330.

The Kaarta Stencil 2 [87] uses a Velodyne VLP-16 Puck lidar scanner, a MEMS-based inertia measurement unit, and a gray-scale camera that was not activated during our tests because it is less reliable in irregularly lit underground conditions. The Stencil 2 is based on Lidar odometry and mapping (LOAM) SLAM [95], enabling mapping of environments without using external global referencing systems such as ground control points or GPS. The Stencil 2 can nominally collect 300,000 pts/s in single-return mode over a 360° horizontal field of view. The VLP-16 uses 16 channels, with an angular (vertical) resolution of 2.0° and a uniform 30° vertical field of view. Velodyne reports an accuracy of ± 0.03 m and a range of up to 100 m [94].

The Emesent Hovermap can be mounted on various mobile platforms and provides flight assistance and autonomous navigation capabilities to specific UAVs. It utilizes the same sensor as the Karata Stencil 2 and a MEMS-based IMU. An action camera can be attached to colorize point clouds. Hovermap uses an implementation of the WILDCAT SLAM system [96]. Hovermap rotates the lidar sensor 360° along the long axis of the unit at a rate of 0.5 Hz resulting in a near 360° × 360° field of view.

The Faro Focus S 70 is a survey-grade static lidar scanner with a manufacturer quoted range of up to 70 m. It can nominally collect up to 1 M pts/s and provides 1 mm range accuracy and 3D point accuracy of 2 mm and 0.15 mm noise error at 10 m [97]. The Faro 3D x330 has a higher maximum scan range of up to 330 m and equivalent range error and noise specifications [98]. In our tests, the static scan resolution was set to 1/8 and quality to 3x, resulting in 10.9 M points per scan (spaced at ~12 mm) with a scan time of 1.5 min. The scan settings were chosen based on geotechnical practitioner experience to resemble regular operational use.

3.3 Data Collection

At Mine-A, we collected a primary (i.e., baseline or reference) scan epoch with both the static system and the MLS for the tests for target-level analysis in a 45-m-long section of the mine's production level, including multiple drawpoints and mine pillars. Additionally, we installed a target board with removable targets and a flat reference surface. Three scan stations for static scans were spaced approximately 15 m apart in the center of the drift. We carried out the mobile scans with a vehicle-mounted forward and backward pass at 10 km/h. After recording baseline scan epochs, we introduced changes by simulating shotcrete spalling and removing target board elements. We then recorded a secondary static scan epoch and mobile scans. Static data acquisition, including setup, required approximately 18 min for the three scans required to cover the test environment. Mobile data acquisition (not including the installation on the mine utility vehicle) required 30 s. Additionally, we performed data collection for the site-level convergence detection tests at Mine-A on a bi-monthly interval on nine different dates. Data were collected similar to the target-level test with two

passes at about 5 km/h driving speed, allowing us to complete 5 km of mobile data acquisition in about 1.5 h.

At Edgar, we performed data collection using the static FARO x330, the Emesent Hovermap, and Stencil 2 MLS in a handheld fashion for target- and site-level tests. MLS scans were collected at an average walking speed of approximately 3–5 km/h. We collected static scans 10 m apart for site-level analysis and aligned them to existing mine survey data using spherical targets. We collected two scan epochs for rockfall detection tests at Edgar, one baseline and one post-change scan for a structured and unstructured scene. Rockfall was simulated by placing rocks of multiple sizes at known locations within the scene.

3.4 Data Processing and Analysis

Static lidar and MLS require post-processing before generating statistical analysis and quality metrics. Figure 1 shows the flowchart of the data processing and analysis process we followed in this study.

After data collection, we used manual coarse registration to align static data for initial positioning and survey target alignment at Edgar. Then, we used iterative closest point (ICP) registration for scan-to-scan fine registration in CloudComapre [99]. For alignments of site-wide static scans, we utilized the "Global Registration" function in Maptek PointStudio [100] as it allows a combined ICP registration

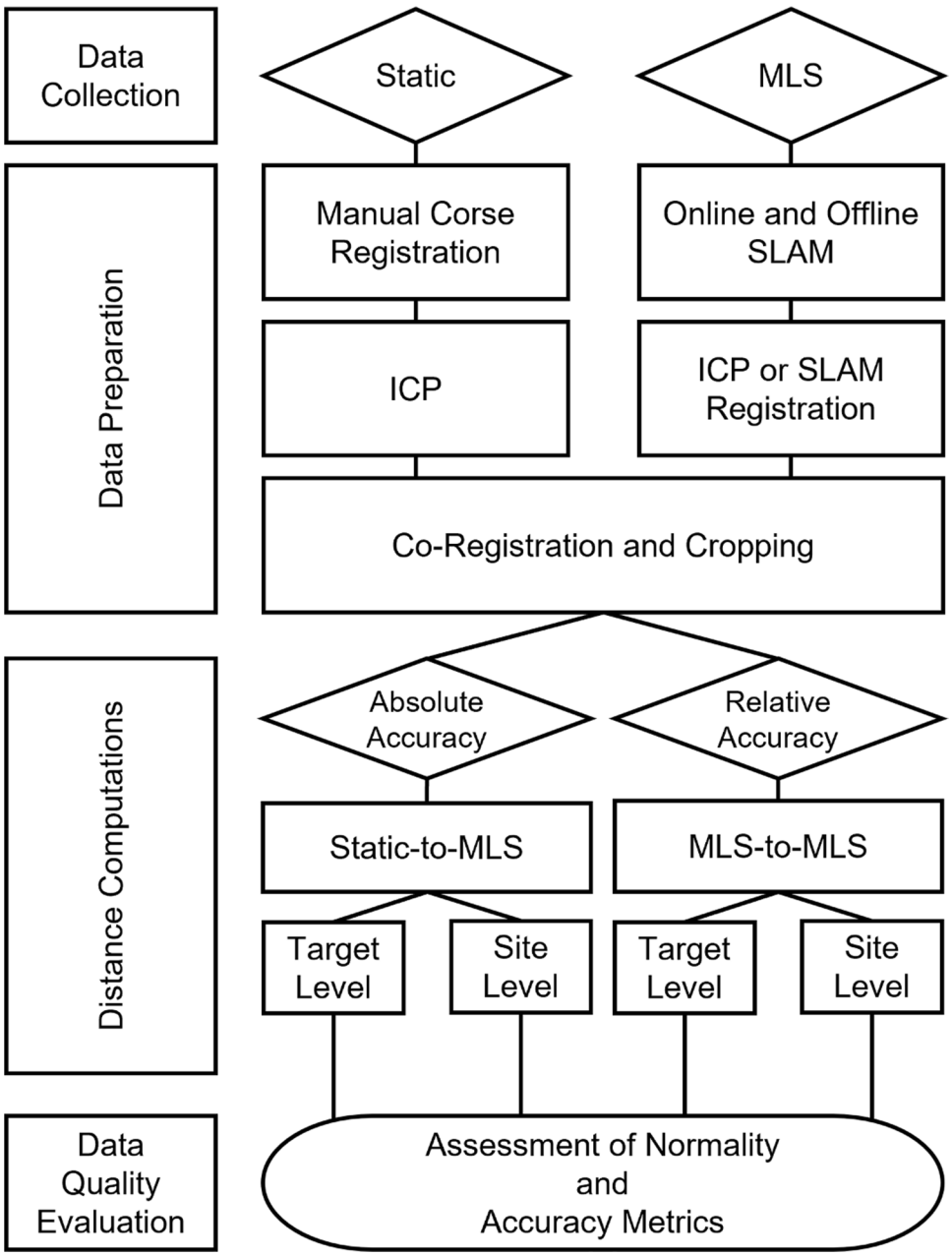

Fig. 1 Flowchart of our test methodology

of multiple scans and the use of survey target constraints. Both Stencil 2 and Hovermap utilize their proprietary SLAM engine and software package for real-time processing and initial post-processing to generate point clouds. For co-registration, we used manual transformation followed by ICP. We tested different alignment methods for site-level accuracy, including rigid, global alignment (GLO), an ICP constrained to the start of the MLS scan to highlight drift versus surveyed scans (ENT), pseudo-non-rigid alignment using 10-m segmented (SEG), and SLAM-based iterative closest point algorithms.

For SLAM-based processing, Mine Vision Systems' proprietary software allows for in-field alignment of scan data to a base map for our bi-monthly data collection at Mine-A. Emesent's processing software was used with default settings to output loop-closed and non-loop-closed datasets. The "merge" function was only used to generate data for the SLAM-based registration accuracy tests. We then cropped the data based on the tested variable and associated quality metric.

For distance calculations, we utilized cloud-to-cloud (C2C), cloud-to-mesh (C2M), and multi-scale model to model cloud comparison (M3C2) implemented in CloudCompare [99]. Meshes were generated at a 0.01-m resolution. For M3C2 parameters at least 20 times larger than surface roughness, normal scales were selected at 2–3.0 m in 0.5-m increments [101]. The projection scale was set to 0.5 m and the maximum projection depth to 1.0 m. C2C, C2M, and M3C2 distances were then exported for analysis in R-Studio [102].

4 Results

4.1 Assessment of Normality

Our initial data exploration found that our accuracy metric for Stencil 2 and Hovermap, static-to-MLS distance (Appendices 1 and 2), does not conform to a Gaussian distribution for most datasets. A high quantity of large outliers causes high kurtosis, while skewness is low for most C2M distance distributions but significantly higher for all M3C2 distributions. The Q-Q plots and histograms for our data in Figure 2 confirm this observation. High positive kurtosis is most prominent for rough surfaces common in underground mining environments, while distance measurements on flat surfaces show much closer Gaussian conformance based on their kurtosis and skewness. The distribution of M3C2 distances also shows higher kurtosis for all scenes than the distribution of distances calculated by C2M. The difference between M3C2 and C2M is most significant for rough surfaces. Kurtosis is on average 4 times higher for distance distributions of

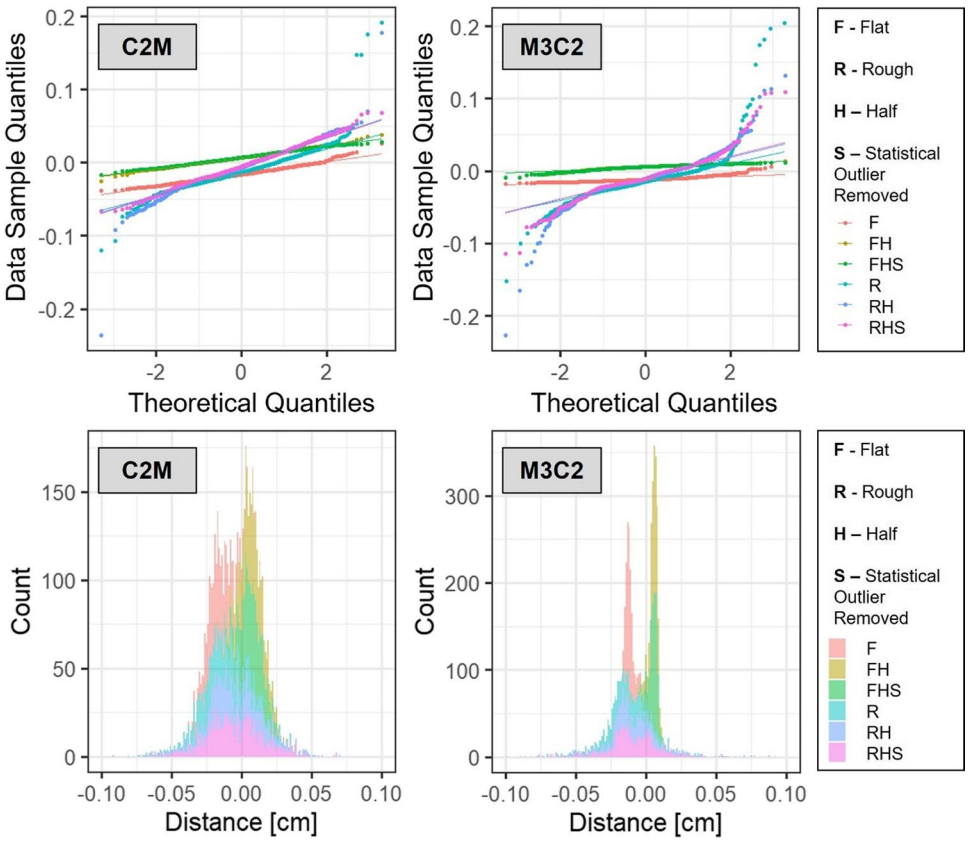

Fig. 2 Q-Q plots and histograms for the Stencil 2 mobile lidar system vs. static lidar distances by scenes for cloud-to-mesh and multi-scale model to model cloud comparison computations based on 1000 random samples for each scene

rough surfaces compared to those of flat surfaces when using M3C2, while only being 2 times higher for C2M-calculated distance distributions. Statistical outlier removal (SOR) filtering proves highly effective in removing outliers in both flat and rough C2M distance distribution, resulting in good normal distribution conformance of MLS errors.

4.2 Data Collection Efficiency

Table 3 highlights the efficiency of MLS compared to static lidar scanning. The total number of points in each of the two MLS datasets is about 80 % lower than the number of points in the static dataset. As MLS data collection is 30 times faster, the effective sampling rate measured in points per second is approximately five times higher than the rate for the static system. This is likely a lower-bound estimate, as time requirements for static scanning can increase if scans are interrupted, larger scanners and more elaborate leveling procedures are used, and the time for moving between scans is considered.

Subsampling is commonly applied as a post-processing step to reduce and standardize the point cloud density. The result is a more consistent sample distribution and improved computational efficiency. Figure 3a illustrates the decay of the number of points as a function of the subsampling minimum point for static and MLS point clouds. A 0.5-cm minimum spacing does not significantly reduce the MLS data. The static dataset is reduced from 26 million to less than eight million points, with only 30% of the initially collected data remaining. Subsampling to a 1-cm minimum spacing commonly used at Mine-A for geotechnical applications only retains three million points of the original 26 million static points (approximately 10%), resulting in fewer points than the MLS at the same subsampling level. The sensitivity of static data to subsampling is primarily caused by the large variations in point cloud density as a function of distance from the scanner shown in Figure 3b. If the subsampling is increased beyond 2 cm, the point reduction rate becomes more linear, and the total number of static lidar points approaches the total number of points in the mobile clouds.

4.3 Density and Coverage

Table 4 summarizes the spatial distribution of static and vehicle-mounted MLS data collected at Mine-A. The relative regional distribution of points between the systems is comparable. The static system and Hovermap collect about

Table 3 Point collection efficiency of static lidar and two MLS

	Faro Focus S70	Stencil 2	Hovermap
Trajectory length (m)	45 (single pass)	2 × 45 (in and out)	2 × 45 (in and out)
Trajectory time (s)	900	30	33
Avg. speed (km/h)	0.18	10.8	9.7
Total points (M)	26.1	4	5.2
Points per second (pts/s)	29,000	133,333	156,000

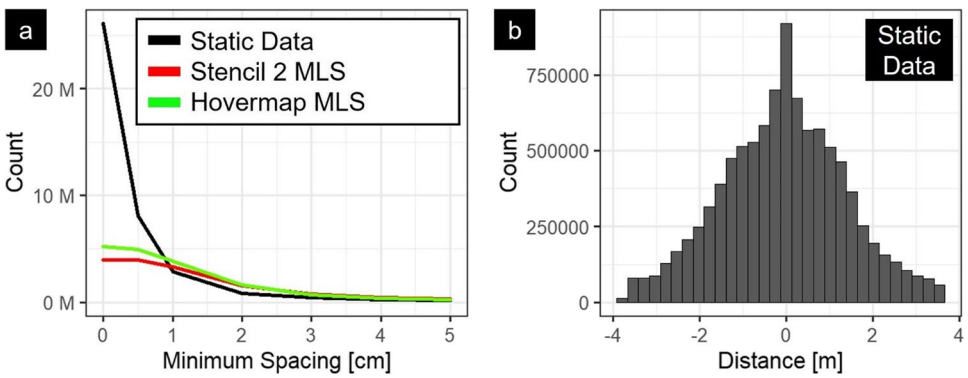

Fig. 3 Effect of subsampling on total points for static and mobile lidar systems Stencil 2 and Hovermap (**a**) and histogram of static point cloud density as a function of distance to the scanner (**b**)

Table 4 Comparison of point distribution between three static lidar scan stations and MLS with Stencil 2 and Hovermap mounted to a mine buggy

	Faro Focus S70		Stencil 2		Hovermap	
Ground points (M)	6.7	26 %	1.1	28 %	1.2	23%
Rib points (M)	8.2	31 %	1.7	43 %	1.9	37%
Roof points (M)	11.2	43 %	1.2	30 %	2.1	40%
Total points (M)	26.1	100 %	4	100 %	5.2	100%

40% roof points, compared to the Stencil 2, which collects the highest proportion of drift rib points (43%) out of all systems, but only 30% roof points. Hovermap data only shows a 3% difference between the number of points on the ribs and roof. Hovermap also collects the lowest proportion of ground points (23%) from all systems.

Figure 4 shows the density of the point clouds generated by the static scanner compared to the two MLS at 10 km/h. The color scale indicates the number of volumetric neighbors calculated in a spherical radius of 2 cm, from low to high (blue, green, yellow, orange, red). Static scan point density decreases exponentially with distance from the scan station as 91% of data are collected within a 5-m radius (Figure 4b). Out of these points, 20% are collected in a 7 m^2 area in immediate proximity to the scanner. Point density and coverage significantly decrease beyond a 5-m distance to the scanner, with occlusions impeding a correct representation of most surfaces. The density of both MLS point clouds remains constant at around 8000–10,000 pts/m^2 for wall segments 1 m above the floor and 10 km/h driving speeds. Figure 4c, f, and i also show that the sampling patterns vary significantly between each system. The static scanner generates a regularly spaced sample grid while the non-rotating Stencil 2 samples in a diagonally crossed scan line pattern. This pattern results from the angled scanner orientation and the back- and forth pass. The Hovermap's rotating sensor produces a more even point distribution with less pronounced scan lines.

The complex and confined geometry of mine drifts often causes occlusion, i.e., reduced coverage in static scan point clouds of more complex scenes like the mine pillar shown in Figure 5a. The pillar is located between static scan stations III and IV, as shown in Figure 4a. Although station III is located 5 m to the pillar's left, the line of sight is occluded so that only points from station IV, which is 10 m to its right, cover the area highlighted in the red box. Figure 5d shows the significantly denser point cloud from the MLS.

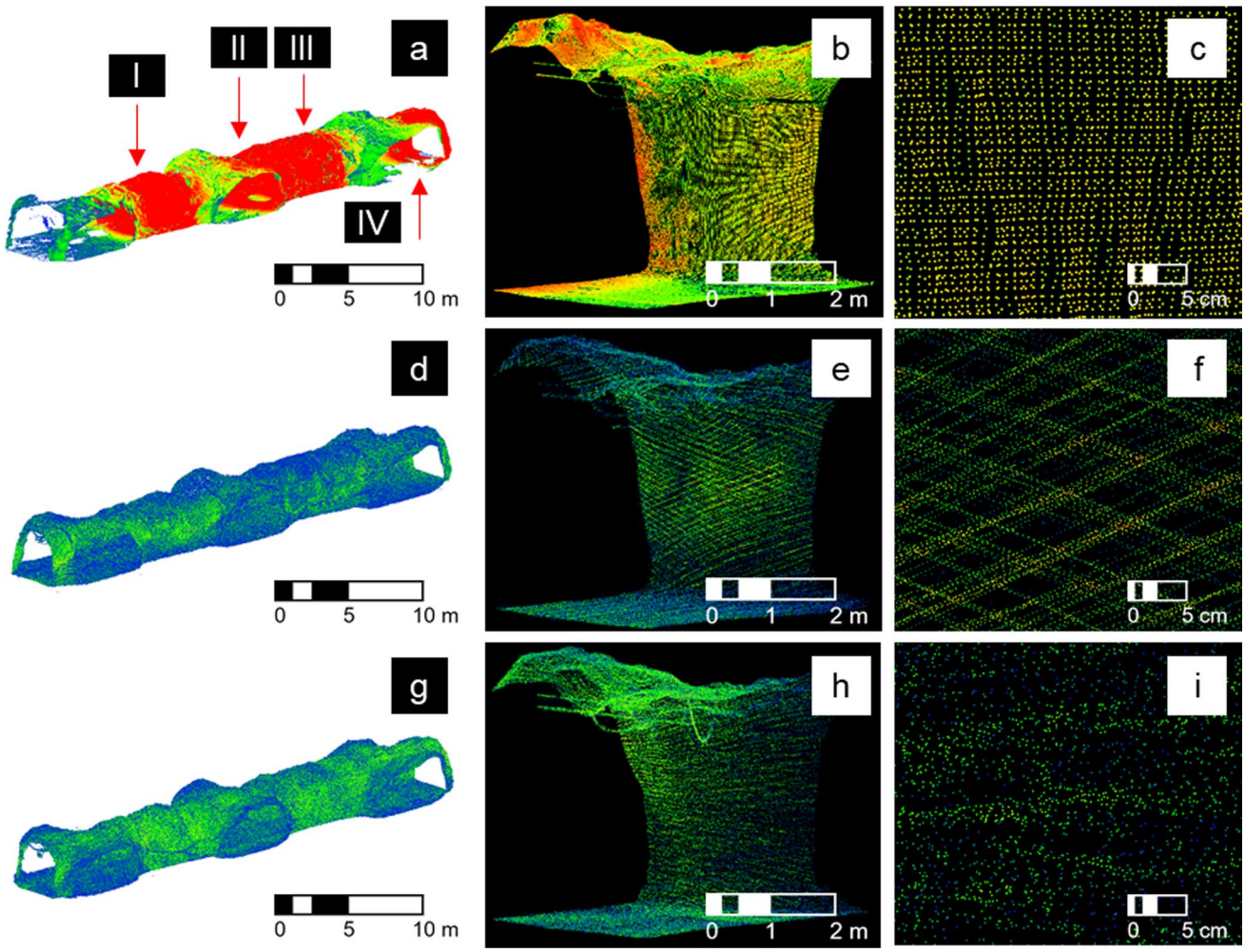

Fig. 4 Coverage and density difference between static lidar (**a**, **b**, **c**) and mobile lidar systems Stencil 2 (**d**, **e**, **f**), and Hovermap (**g**, **h**, **i**) point cloud data. Color scale indicates increasing density from blue, green to red. Arrows indicate static scan station locations

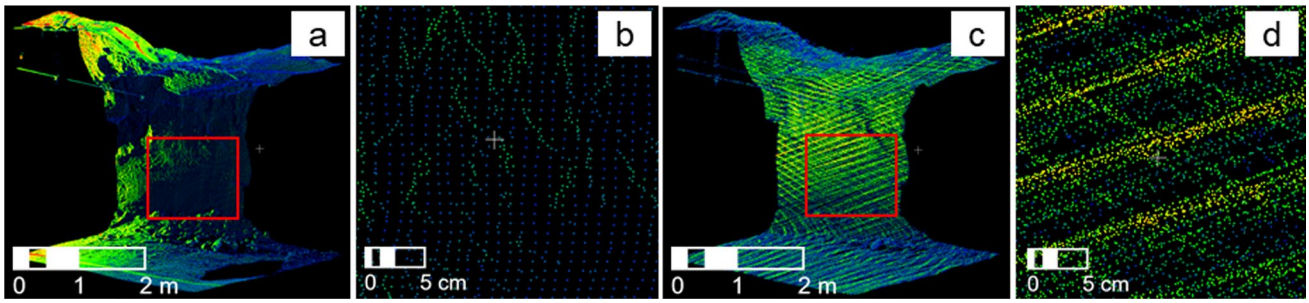

Fig. 5 Coverage and density difference between static lidar (**a**) and Stencil 2 mobile lidar system (**c**) point cloud data on a mine pillar and zoomed view of the red box in (**b**) for static and (**d**) for mobile lidar

4.4 Absolute Accuracy

We calculate target- and site-level absolute trueness and precision to determine MLS absolute accuracy compared to static lidar ground-truth data. The target-level data are shown in Appendices 1 and 2. In our tests of target-level absolute trueness at Mine-A and Edgar, the maximum mean and median values are 1.58 and 1.65 cm, respectively. The Hovermap datasets show lower mean and median values at 0.75 cm and 0.72 cm, respectively. Both systems' target-level trueness metrics stay well within the sensor's quoted accuracy of ±3.0 cm, indicating that SLAM processing does not negatively affect data trueness. For an analyzed cross section of the Stencil 2, most points fall into the ±3.0 cm sensor accuracy envelope, but we can observe a bias towards measurements >3.0 cm compared to the static reference data (Fig. 6). This finding is consistent with the analysis of the complete dataset showing a maximum mean and median of 1.5 cm. Registering only half of the drift surface resulted in mean and median values decreasing to a maximum of 0.71 cm, closely resembling the values derived for the Hovermap datasets. Using a statistical outlier removal filter in CloudCompare only marginally improved the target-level trueness of Stencil 2 data.

For our target-level absolute precision test at Mine-A and Edgar, we evaluate absolute precision by standard deviation σ and mean absolute deviation MAD of the distances between MLS and static data. Standard deviation and MAD for Stencil 2 data ranged from 0.23 to 2.15 cm and from 0.2 to 1.62 cm, respectively. For Hovermap data, σ ranged from 0.44 to 1.31 cm and MAD from 0.4 to 1.03 cm. While all precision metrics stay within the sensor's quoted range accuracy of ±3.0 cm, M3C2-based metrics stay well within a ±1.5 cm envelope. Absolute precision shows an order of magnitude of difference between flat and rough surfaces for both MLS, with a minimum MAD of 0.2 cm for the flat surfaces and a maximum σ of 2.15 cm for the rough mine drift walls. On average, σ and MAD, when measured by M3C2 distances, are 48% lower than the equivalent metric derived by C2M. This difference is 46% higher for distances between flat surfaces than for those between rough surfaces. These differences highlight the significance of the chosen calculation method on the derived precision metric. C2M tends to be more reliable on flat surfaces, while M3C2 usually performs better on surfaces with varying roughness. Therefore, we compare C2M for flat (0.85 cm MAD) and M3C2 for rough (1.01 cm MAD) and reveal a much smaller difference in the MAD as a metric for MLS precision. It is important to note that the standard deviation and MAD of distances as an estimator for MLS data precision are impacted by the MLS and static data precision and the precision of the change calculation algorithm.

As part of our site-level absolute trueness and precision test, we investigated the consistency of ICP alignment results of 170 m of MLS data to surveyed static data in Maptek Point Studio and CloudCompare. Based on nine outputs, 3 in CloudCompare, 3 in PointStudio with and three without "Smart Sampling" enabled, the average median error between

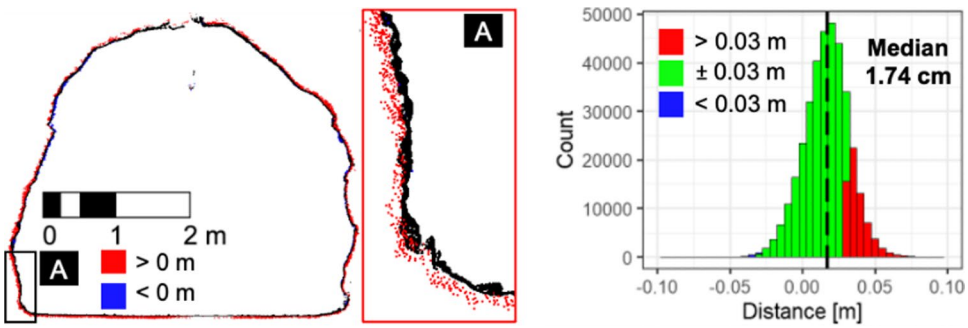

Fig. 6 Cross section of cloud-to-mesh comparison showing range bias of mobile lidar system data registered to static (black) data and histogram with a zoomed section in (A)

MLS and static data is 1.2 cm with a MAD of 6.9 cm and minor static-to-MLS distance deviations between all runs. ICP generally results in globally optimal trueness and precision within the accuracy constraints of the sensor while being repeatable with low deviations between outputs and software. Figure 7 shows a representative section of the data after global ICP alignment. The MLS data are shifted to the right of the surveyed static data with red and blue points indicating cloud-to-mesh differences larger than the sensor's quoted range accuracy. The distribution of the differences resulting from global ICP (GLO) is also visible in the histogram.

Although the GLO ICP process results in a globally optimal alignment as measured by the root mean square error (RMSE), it obscures drift error common to MLS data. Figure 8 shows the drift error as it increases over the trajectory length in the entry-aligned data (ENT) in both the visual representation and the plot of the mean and MAD of the C2M differences. The mean distance deviation at 150 m is 0.18 m or 0.12% of trajectory length. As Figure 8 shows, the segmentation-based method (SEG) effectively reduces the increasing error seen in the ENT data. As seen in the SEG histogram, this method significantly increases the number of points falling within the sensor accuracy envelope and reduces the number of points in the data tails.

4.5 Relative Accuracy

Our analysis of relative target-level trueness and precision based on M3C2 distances is documented in Appendix Table 9. The skewness values are close to 0, and kurtosis is close to 3 after SOR filtering for all datasets, indicating good normal distribution conformance. Relative trueness ranges from 0.22 to 0.25 mm (mean) and from 0.07 to 0.43 mm (median) for Stencil 2 and from 0.25 from 0.58 mm (mean) and from 0.07 to 0.68 mm (median) for Hovermap. Relative precision ranges from 3.4 to 13.21 mm (σ) and from 2.9 to 6.7 mm (MAD) for Stencil data and from 4.96 to 8.24 mm (σ) and from 2.92 to 6.55 mm (MAD) for Hovermap data. Relative accuracy metrics are significantly better than the lidar sensor's range accuracy envelope. When comparing absolute and relative accuracy on a target level for rough surfaces, Table 5 suggests significantly higher relative trueness and precision. Trueness is at least 14 times higher, while precision is at least 1.4 times higher.

For site-level precision tests at Edgar, we tested the intrinsic and extrinsic SLAM precision and loop closure of the Hovermap MLS. Table 6 shows the results of our intrinsic and extrinsic precision tests. Q-Q plots and kurtosis/skewness show that distances between two clouds do not follow a normal distribution. Intrinsic precision evaluated by median and MAD is very similar for both loop (INL), and non-loop-closed (INN) surveys with medians of −0.21 cm and 0.05 cm and MAD of 2.73 cm and 3.21 cm, respectively. Loop closure lowers the stander deviation significantly from 7.11 to 2.86 cm. Extrinsic precision is measured by comparing a baseline scan against scans following the same trajectory direction (SD) and the opposite direction (OD). The test results show that the precision of MLS data varies depending on the chosen scan trajectory. Scans carried out in opposite directions result in significantly higher median (−0.66 cm) and MAD (10.30 cm) values for distances between the two scans, compared to scans carried out in the same direction with a median of −0.08 cm and MAD of 4.26 cm.

4.6 Loop Closure and SLAM Registration Quality

We tested loop closure and SLAM-based registration in more detail using a 650-m-long scan trajectory at Edgar. Figure 9 shows the C2M distances between two SLAM outputs of the same scan dataset on a 650-m-long trajectory, with distances exceeding the quoted sensor range accuracy of ±3 cm colored in red and blue. Both the loop and non-loop trajectories show regions with a concentration of point distances outside the ±3 cm sensor accuracy envelope. The

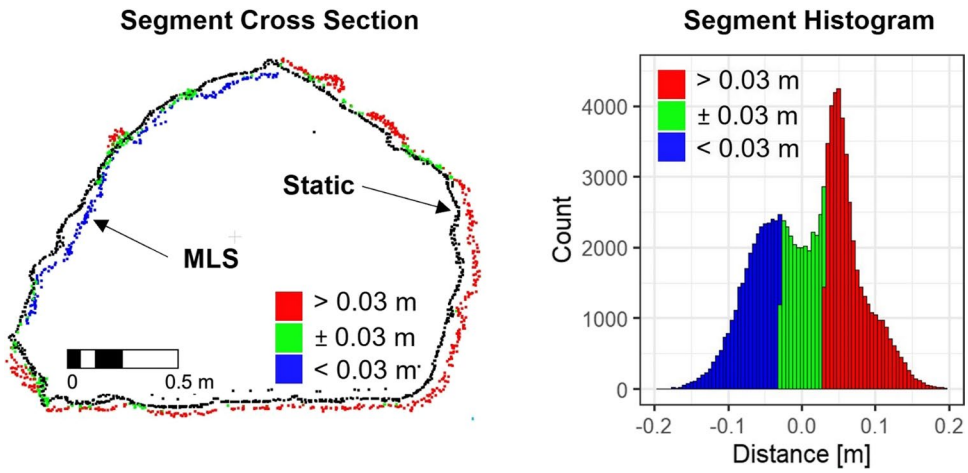

Fig. 7 Identification of SLAM drift error using a cross section and histogram showing a shift of MLS data compared to static data when using global ICP

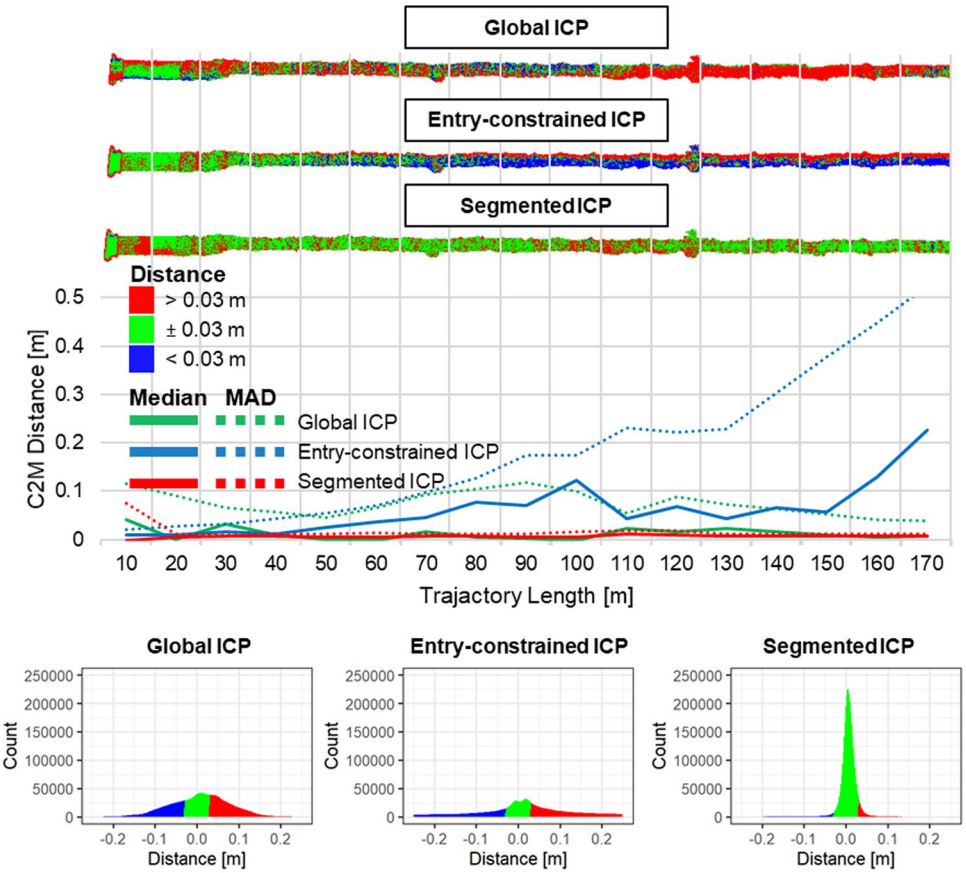

Fig. 8 Visual comparison of global, entry-constrained, and segmented ICP and mean and MAD over trajectory length and histograms

Table 5 Comparison of absolute and relative accuracy metrics based on M3C2 distances

	System					
	Hovermap			Stencil 2		
	Absolute[1]	Relative[2]	Factor	Absolute[3]	Relative[4]	Factor
Mean [mm]	7.50	−0.25	30.00	7.10	−0.22	32.27
σ [mm]	12.70	5.16	2.46	19.00	13.21	1.44
Median [mm]	7.20	−0.07	102.86	6.30	−0.43	14.65
MAD [mm]	6.10	2.92	2.09	14.60	6.68	2.19

[1]Data from Appendices Table 8 and 9—Rough M3C2. [2]Appendix Table 9—Hovermap 5m. [3]Appendix Table 7—RH M3C2. [4]Appendix Table 9—Stencil 2 5m

density plot in Figure 9 confirms the higher accuracy of loop-closed scans. The non-loop-closed scan shows a higher density of points with distances < ±5 cm.

To evaluate the effect of loop closure on absolute accuracy, we registered the previous MLS data to our static data for the first 240 m of drift by using a 30-m-long section at the beginning of each scan. Figure 10 highlights that the loop-closed scan trajectory conforms better with the surveyed static data than the non-loop-closed scan. We can observe a difference of up to 1.0 m in horizontal drift and 0.5 m in vertical drift in the non-loop-closed data. The loop-closed data shows a maximum of 0.25 m of horizontal difference and less than 5.0 cm of vertical difference from the survey data. This is a 75% decrease in drift horizontal drift error and a decrease of 90% in vertical drift error.

Besides loop closure, SLAM-based registration can significantly reduce drift error in point clouds by utilizing a baseline scan to align new scan epochs and constrain the SLAM algorithm. Figure 11 shows the results of SLAM-based alignment using the Stencil 2 and Mine Vision Systems' SLAM solution to align MLS data to our surveyed, static data. We cannot observe systematic drift error, and differences between static and MLS data are comparable to the target-level accuracy of the system. The site-level accuracy metrics reflect the registration quality with very high trueness (median: 0.4 cm) and precision (MAD: 2.9 cm) close to the

Table 6 SLAM precision for Hovermap data measured by C2M in cm

	Intrinsic		Extrinsic	
	INL	INN	EXN, OD	EXN, SD
Points	14.1M	14.5M	3.3M	2.5M
Mean (cm)	−0.20	0.23	−0.41	0.06
σ (cm)	2.86	7.11	11.01	5.94
Median (cm)	−0.21	0.05	−0.66	−0.08
MAD (cm)	2.73	3.21	10.30	4.26
Kurtosis	17.17	10.45	3.21	13.29
Skewness	−1.01	0.22	0.12	0.22

INL, intrinsic, loop; INN, intrinsic no loop; *EXN, OD*, extrinsic no SLAM registration, opposite direction; *EXN, SD*, extrinsic no SLAM registration

sensor's quoted range accuracy. Utilizing Emesent's software for SLAM-based registration of two consecutive Hovermap scans of the same unchanged scene resulted in even higher accuracy with a median of 0.05 cm and MAD of 1.36 cm.

4.7 Rockfall and Convergence Detection Field Tests

Our field tests also evaluated artificial changes, simulated failures, and naturally occurring changes in underground mine drifts at Mine-A and Edgar. Figure 12 compares the detectability of four types of changes in static and Stencil 2 MLS data in an underground mine production area. Using C2C distance calculations between a pre- and post-change epoch, we can identify changes in artificial targets (A), a 15-cm-tall piece of rock placed on a boulder (B), simulated rockfall from the roof of the drift (C), and rock debris accumulation on the mine drift floor caused by the rockfall with individual fragments as small as 5 cm in diameter (D).

Figure 13 shows two tests using Hovermap data to evaluate the detectability of rock fragments in a size range typical for minor geotechnical failures that could be a potential precursor of a more significant event. In the structured scene in Figure 13a and b, we can make out all six rocks with the smallest (6) measuring about 2.5 × 5 cm. Four rocks from the structured scene were placed in the unstructured scene in Figure 13c and d. The larger three (1, 2, 5) can be easily detected using C2C, C2M, and M3C2 comparisons. The smallest (6) could not be identified in a C2C comparison, while the C2M and M3C2 analysis resulted in small but noticeable change signatures.

The quality of change detection in scenes with high surface roughness variations and occlusion not only does depend on the density of the data but also is largely impacted by the chosen change detection method. As shown in Figure 14, the normal-based approaches C2M and M3C2 resulted in more false-positive points or noise when compared to C2C. False negatives predominantly occur in areas of lower point density caused by occlusion. As a result, C2M generates false positives due to gaps in the reference mesh and is more prone to incorrectly orientated normals due to the high variability in surface roughness. For example, target (1) in Figure 14 shows data gaps in the center of the rock for C2M, while (A) shows many incorrectly classified points due to the mesh inconsistency.

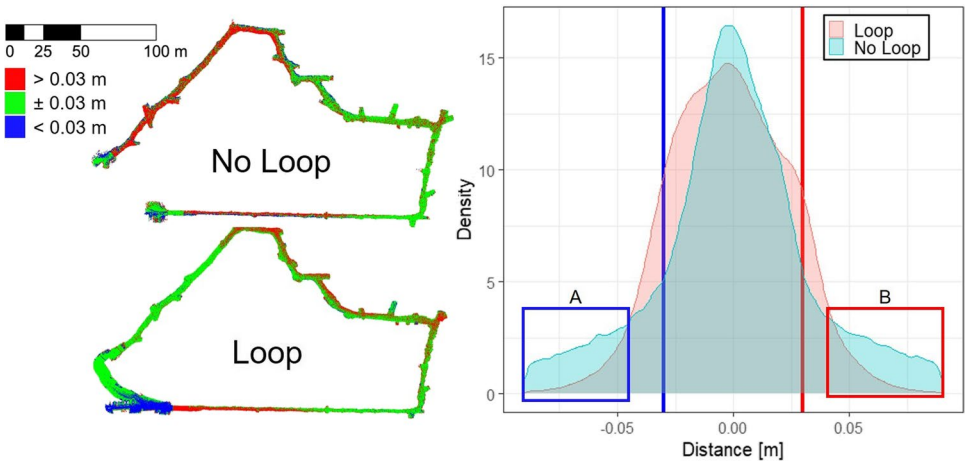

Fig. 9 SLAM intrinsic precision measured by the cloud-to-mesh distance between two SLAM outputs over a 650-m-long mine drift trajectory with and without loop closing

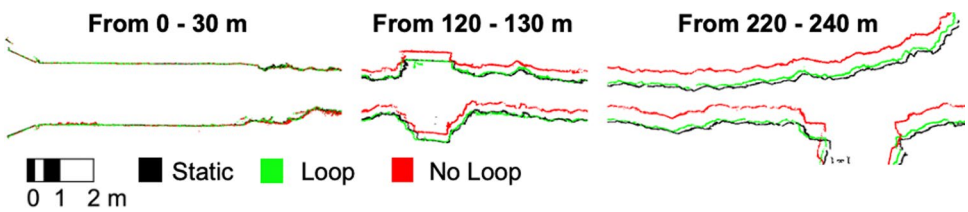

Fig. 10 Top-down view shows the drift error differences between data without loop closure (red) and with loop closure (green) compared to static data (black)

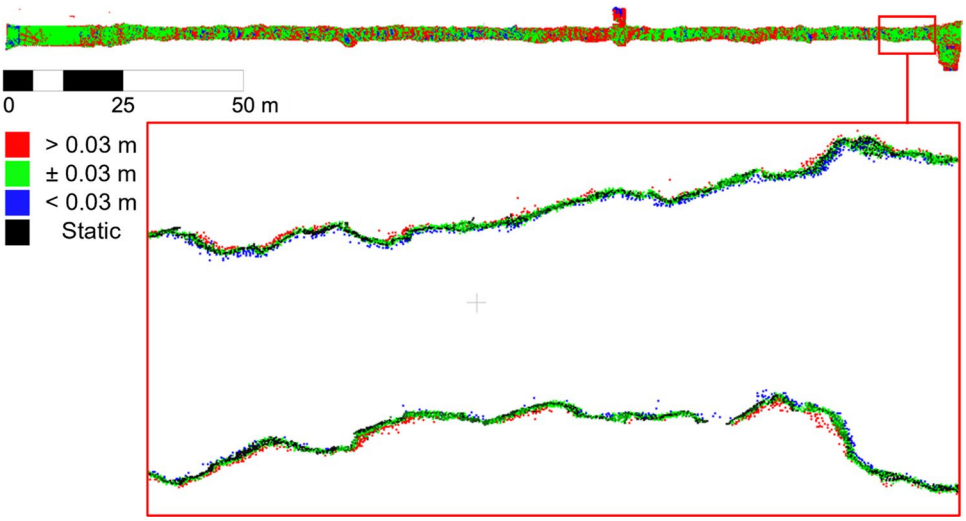

Fig. 11 Top-down view and horizontal cross section of signed cloud-to-mesh distances between Stencil 2 and static data using SLAM registration

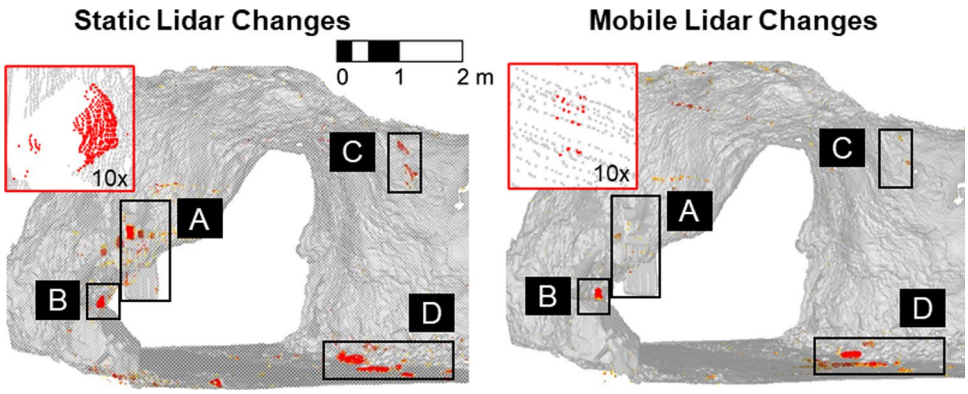

Fig. 12 Overview of a scene with changes in static and Stencil 2 MLS data. (**A**) Target board. (**B**) Placed rock. (**C**) Scaled rock. (**D**) Rockfall debris. Red box: 10x magnified close-up frontal view of (**A**)

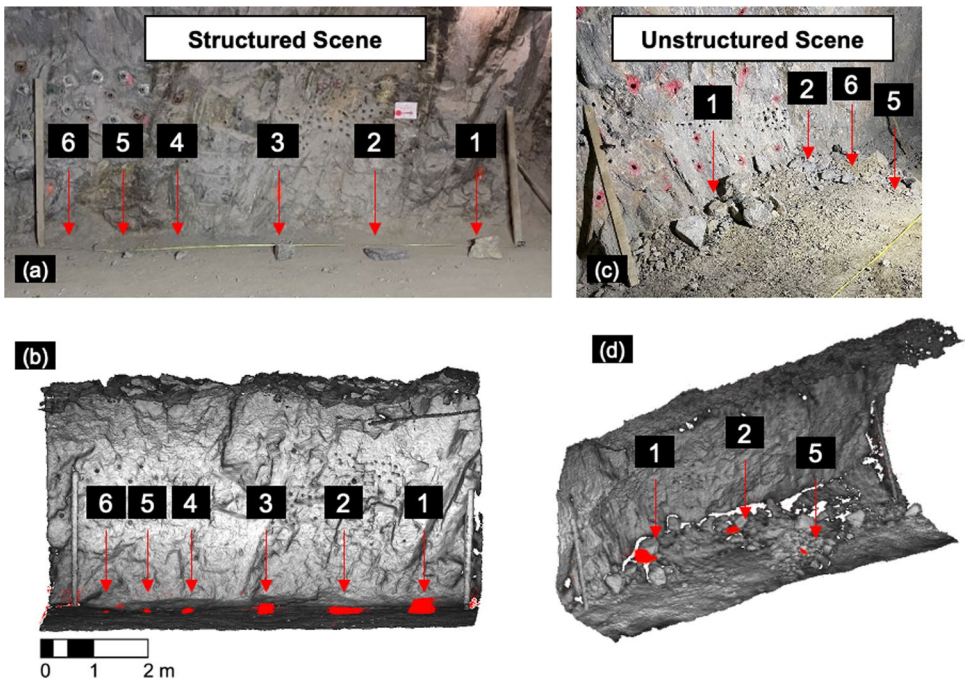

Fig. 13 Test of detectability of progressively smaller rocks 1 (25 × 20 cm)–6 (2.5 × 5 cm) on a flat surface in a structured (**a**, **b**) and unstructured (**c**, **d**) scene with threshold filtered cloud-to-cloud distances

Figure 15 shows an example of our mine-scale convergence monitoring tests at Mine-A. Over 3 months, we can detect significant changes in (A), (B), and (C) based on M3C2 distance computations and an assumed 3 cm limit of detection. Geotechnical engineers at Mine-A confirmed that changes in (A) correlate with the construction of concrete road surfaces and shotcrete work in the mine roof. The changes in (B) represent mining-induced convergence of up to 10 cm (1.0 mm/day) in the mine roof and ribs. Visual and range-finder monitoring confirmed both the magnitude and location of the convergence.

5 Discussion

5.1 MLS Acquisition and Processing Efficiency

Lidar data acquisition needs to be efficient enough to provide sufficiently frequent data updates to be an effective monitoring tool. Efficiency requirements increase as a function of the monitoring area and geotechnical stability. Fekete et al. [103] recognized this by stressing that static lidar scanning needs to limit interference with other underground operations. We show that static lidar data in underground drifts suffers from high point density decay over the scan distance, requiring closely spaced scan stations that result in time-consuming stop-and-go scanning and interruptions of operations. Single-pass static scanning of 2.5 km at Mine-A at an average speed of 0.18 km/h would take about 14 h or about 2 days. A double-pass MLS at 5 km/h requires about 1.5 h. Our tests on target-level accuracy indicate that even higher speeds of up to 10 km/h do not negatively impact MLS trueness and precision, making MLS data acquisition significantly faster than static scanning. Rapid MLS creates new MLS-specific use cases that require higher frequency data collection that can currently not be realized with static lidar data. Such applications could include ground support mapping and monitoring [104], mine ventilation surveying [105], and rock fragmentation analysis [106] in block cave drawpoints.

In our tests, we can see that static lidar data are subject to exponential point-loss by subsampling. Jones et al. [83]

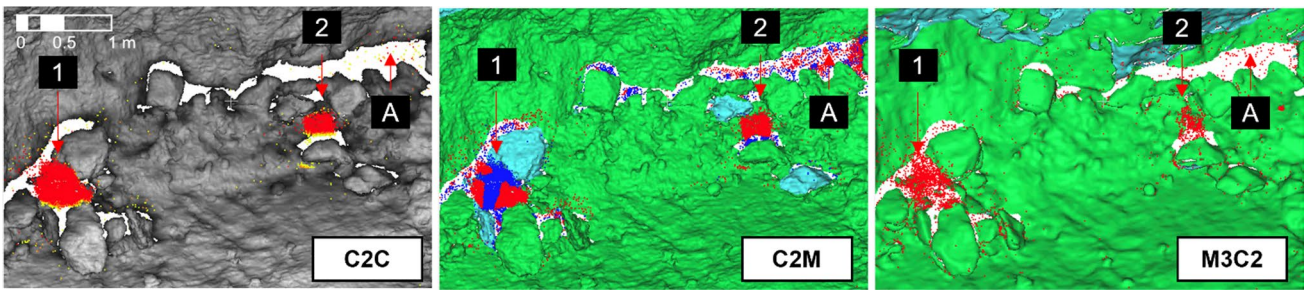

Fig. 14 Filtered distances (>3 cm) in red showing noise for cloud-to-cloud, cloud-to-mesh, and multi-scale model to model cloud comparison. More noise at (A) due to non-closed mesh and errors on (1) due to incorrect normal orientation (cyan) in cloud-to-mesh

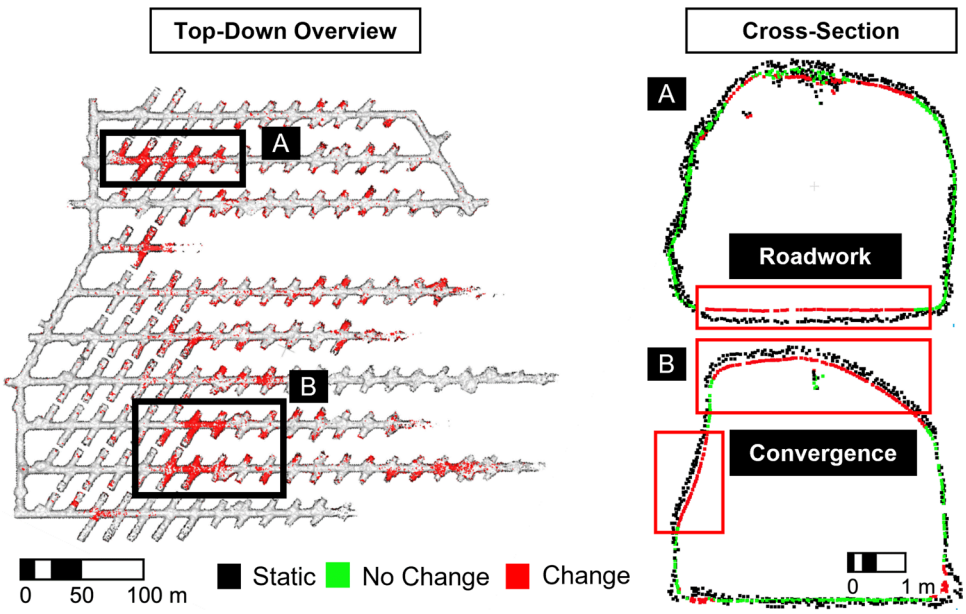

Fig. 15 Results of SLAM MLS survey at Mine-A with Stencil 2 with significant changes classified by and multi-scale model to model cloud comparison distance calculation

highlighted the importance of uniformity of point cloud density for underground applications, and Gallwey et al. [104] described challenges due to oversampling of surfaces close to a static scanner. MLS achieves a more consistent point spacing, a five times higher effective sampling rate than static lidar, and maintains almost 10 times as many points when applying a common subsampling spacing of 1 cm. So far, the potential of SLAM-based MLS to alleviate these limitations could only be inferred from previous studies [52, 59, 61].

While the efficiency of MLS data collections offers various opportunities, dynamic underground mine environments can make the execution of complex and repeatable MLS survey trajectories challenging. In our experience, planning surveys on days with lower operational activity while increasing the monitoring frequency to ensure sufficient coverage and consistent trajectories in critical areas is beneficial. Higher speed and efficiency scanning also reduces data collection costs and improves the parallelization of operational and monitoring tasks. Integration of MLS with mining equipment presents an opportunity to reduce friction between operational and monitoring tasks. While MLS outperforms static scanning in data acquisition speed, traditional post-processing and evaluation methods are not optimally suited for the unique MLS data properties, namely higher data volume and lower lidar sensor accuracy. Accordingly, we believe there is significant further potential for workflow improvement for processing and analysis of mine-scale high-frequency MLS monitoring. With that said, we note that mine-scale monitoring using static laser scanning is also associated with significant post-processing requirements, most notably the need to co-register point clouds collected from multiple scan positions.

5.2 MLS Data Accuracy

Our evaluation of MLS accuracy combines non-parametric statistics with target- and site-level data analysis previously deployed separately by authors like Sofonia et al. [90] and Toschi et al. [92]. We also investigate traditional absolute accuracy and monitoring-relevant relative accuracy metrics. We found this approach well suited to evaluate outlier-heavy MLS datasets and clarify reporting and discussion of monitoring-centric accuracy metrics. For the first time, our work presents a systematic comparison of static-to-MLS data in multiple underground mining environments using multiple MLS and high-accuracy static lidar reference data.

At a target-level, both tested MLS operate within the sensor-specific accuracy envelope of ±3 cm, with most datasets showing conformance within a ±1.5 cm trueness envelope compared to static lidar data. Both systems' absolute target-level precision remains below a MAD of 2 cm, with M3C2-derived MAD values of 1 cm. These metrics align well with reported findings in previous studies. Sofonia et al. [90] reported between 2 and 3 cm of root mean square error (RMSE) for UAV-MLS-to-static data collected at a 10–20 m range, and Hößelbarth et al. [81] and Frangez et al. [56] reported 0.7–8.6 cm of target error with an earlier generation SLAM-based MLS deployed in underground openings. Our results confirm that sensor range accuracy is the primary limiting factor of target-level MLS data accuracy, while SLAM processing does not introduce any measurable inaccuracy beyond the sensor-specific range noise. Although not observed for both MLS, systematic errors may reduce the data accuracy between different systems.

On a site-level, our tests show that current SLAM-based MLS are prone to three-dimensional drift error. For the first time, we provide quantitative metrics showing that loop closure and SLAM-based registration can significantly improve the data quality for underground geotechnical monitoring. Our Hovermap data showed an average deviation from static survey data of 0.12% of trajectory length. Zhang and Singh's [107] tests of the Stencil 2 in an outdoor, urban environment have shown similar drift error results at about 0.09% [104]. As discussed by Jones et al. [83] and Jones et al. [108], lower drift error will enable longer scan segments when utilizing a segmentation-based ICP approach. Segment length should not exceed the maximum SLAM drift error trajectory length. A 0.12% drift error can accommodate a maximum 25-m scan trajectory before the 3-cm target-level accuracy bound of the lidar sensor is exceeded. To utilize longer scan trajectories for geotechnical monitoring, we show that a pseudo-non-rigid segmentation-based ICP approach can be used to maintain target-level accuracy. Manual processing is often not feasible for large-scale, mine-wide monitoring while also not leveraging additional positional and data quality information that can be utilized in a consistent, fully non-rigid SLAM-based registration process.

For the first time, our experiments demonstrate that state-of-the-art loop closure detection can reduce drift error in underground MLS data by up to 90%. This significantly improves site-level accuracy of underground MLS data collection, especially in mining environments with grid-based drift layouts providing opportunities for loop closures. In addition to loop closure, we found that state-of-the-art SLAM-based registration can further improve site-level data accuracy. Although manual segmentation-based registration approaches, described by Jones et al. [83], can reduce SLAM drift error, they require time-consuming and error-prone user input. They are therefore not ideally suited for frequent, mine-wide applications. Using fully automated SLAM-based alignment of two MLS scans, we could achieve sub-millimeter trueness and precision of 1.36 cm (less than half the quoted sensor range accuracy) while eliminating scan-to-scan drift error. Registering an MLS scan to a static reference scan resulted in slightly worse but still very high accuracy. We achieved absolute trueness and precision of 0.5 cm and 2.9 cm, respectively. For the first time, we show that current generation SLAM systems deliver

high-accuracy, multi-epoch geotechnical monitoring data when localizing to a georeferenced base map or consecutive MLS scan even without ground control points (GCPs). While the registration error using a GCP approach presented by Kumar et al. [109] was significantly higher at 50 cm, we believe that future SLAM systems will likely utilize GCPs to constrain the site-level optimization, enabling longer survey trajectories with less drift and less manual processing to achieve better site-level accuracy. Site-level overfitting remains a concern in environments that experience global shifts of drifts in the rock mass. In the future, robust methods of detecting non-stable GCP and SLAM overfitting could become more relevant research topics.

While absolute accuracy metrics show MLS data's high absolute trueness and precision, we argue that relative accuracy is the more relevant metric for evaluating the quality of MLS data for monitoring applications. Relative accuracy metrics for the Hovermap MLS are almost an order of magnitude better than absolute accuracy metrics. Sub-millimeter relative precision and millimeter relative trueness are consistent with Evans' [110] and Jones et al.'s [14] accuracy estimates using the Hovermap MLS for underground convergence monitoring. The difference between absolute and relative accuracy highlights the need to use task-appropriate metrics. We find that local averaging-based distance computations like M3C2 can significantly improve the relative precision of MLS data. This is consistent with Walton et al. [40], who state that the high density of static lidar data can be exploited to improve the precision of change detection [38]. An example is illustrated in Figure 16. M3C2 was applied to improve relative precision using two identical copies of the MLS point cloud to perform local averaging as described by Lague et al. [101].

5.3 MLS-Based Mine-Scale Geotechnical Monitoring

Our work presents the first use of MLS data to detect small-scale discrete geotechnical failures in underground mines. We could successfully and repeatedly detect rockfall as small as 2 cm in high-density MLS data. While C2M computations can produce ambiguous results under mining-specific conditions due to the high variability in surface roughness and resulting uncertainties in normal orientations, M3C2 distance calculations are better suited to capture discrete failures. These observations align with DiFrancesco et al. [111], who recently showed the effectiveness of M3C2 for rockfall detection on rock slopes. While we showcase the initial potential of MLS-based rockfall detection using manual workflows, future advances in change detection and classification could enable mine-wide rockfall data as a novel monitoring and predictive tool for geotechnical hazard detection. We also demonstrate the efficacy of muli-epoch MLS data. Combined with M3C2-based change detection, MLS enables mine-wide identification of geotechnically and operationally significant changes like convergence, ground support rehabilitation, and road construction. Previously, Iannacchione et al. [112] have used MLS data to verify meter-scale observations of roof failures in pre-defined study areas of an underground limestone mine. For the first time, our study could demonstrate the ability of MLS to generate geotechnical monitoring data with centimeter accuracy on a mine-wide, multi-kilometer scale. Compared to previous use cases with earlier generation MLS and traditional distance computation methods, our results indicate that significantly higher relative MLS data accuracy and limits of detection can be realized on larger, mine-wide scales.

6 Conclusion

With the increasing depth of underground mines, monitoring geotechnical risks becomes more critical. MLS and automated equipment make mobile lidar data more accessible and abundant. Utilizing MLS to improve safety and operational reliability requires a better understanding of SLAM-based MLS data quality. We show that MLS lidar data conforms with or exceeds the required quality to detect geotechnically relevant changes. We show that MLS monitoring can outperform static lidar scanning in target- and site-level coverage, uniformity of spatial sample distribution, and efficiency. In combination with advanced SLAM features like loop closure and scan registration, MLS data have the potential to become an effective and ubiquitous data source for rapid, accurate, and comprehensive geotechnical inspections. More work will be required to test the sensitivity of change detection accuracy to SLAM-based alignment and the possible improvements of site-level accuracy by tightly integrating GCP constraints for the SLAM algorithm. We see potential in developing mining-specific change detection, classification, and data utilization tools that can support the end-users of MLS data in deriving actionable insights.

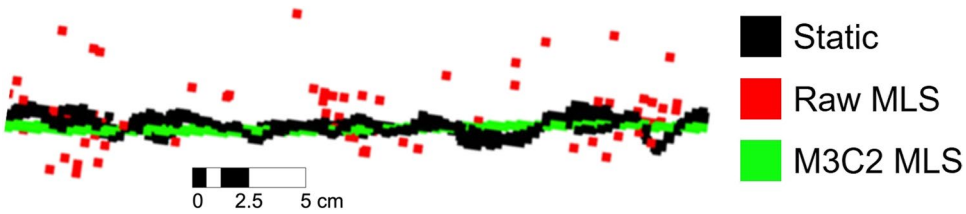

Fig. 16 Top-down view of a mine drift wall segment with multi-scale model to model cloud comparison utilized for point cloud sharpening

Appendix 1

Table 7 Statistical analysis of absolute accuracy of Stencil 2 compared to static data

	F		R		FH		RH		FHS		RHS	
	C2M	M3C2	C2M	M3C2	C2M	M3C2	C2M	M3C2	C2M	M3C2	C2M	M3C2
Points	1020		166,203		1108		86,147		1065		84,250	
Mean (cm)	1.58	1.48	1.31	1.50	−0.70	−0.64	0.61	0.71	−0.71	−0.65	0.59	0.69
σ (cm)	0.87	0.31	1.96	1.67	0.80	0.24	2.15	1.90	0.75	0.23	1.96	1.80
Median (cm)	1.65	1.55	1.38	1.50	−0.69	−0.67	0.71	0.63	−0.70	−0.68	0.69	0.61
MAD (cm)	0.85	0.24	1.62	1.01	0.76	0.20	1.87	1.46	0.75	0.20	1.84	1.46
Kurtosis	4.38	10.87	16.95	60.17	3.33	4.66	9.74	24.33	2.77	4.70	3.62	20.13
Skewness	−0.56	−1.99	−0.96	1.23	−0.08	1.03	−0.28	1.13	−0.05	0.98	−0.06	1.04

C2M, cloud-to-mesh distances; *M3C2*, multi-scale model to model cloud comparison; *F*, flat; *R*, rough; *H*, half; *S*, SOR-filtered

Appendix 2

Table 8 Statistical analysis of absolute accuracy of hovermap compared to static data

	Flat		**Rough**	
	C2M	M3C2	C2M	M3C2
Points	3754		26,682	
Mean (cm)	0.62	0.53	0.72	0.75
σ (cm)	1.04	0.44	1.31	1.27
Median (cm)	0.54	0.52	0.72	0.72
MAD (cm)	0.85	0.40	1.03	0.61
Kurtosis	5.95	5.89	11.27	112.31
Skewness	−0.03	−0.38	−0.28	1.14

C2M, cloud-to-mesh distances; *M3C2*, multi-scale model to model cloud comparison

Appendix 3

Table 9 Statistical analysis of stencil and hovermap relative accuracy with M3C2

	Stencil 2			Hovermap		
	15 m	5 m	SOR	15 m	5 m	SOR
Points	1.5M	553k	544k	5M	1.58M	1.57M
Mean (mm)	0.25	−0.22	−0.23	−0.58	−0.25	0.29
σ (mm)	13.14	13.21	3.40	4.96	5.16	8.24
Median (mm)	0.11	−0.43	−0.07	−0.68	−0.07	0.43
MAD (mm)	6.70	6.68	2.90	3.06	2.92	6.55
Kurtosis	71.31	70.51	4.56	481.72	526.57	5.64
Skewness	−0.05	0.08	−0.22	−0.36	−0.37	0.05

SOR, statistical outlier removal filter

Acknowledgements We want to acknowledge the staff at Mine-A and Lee Fronapfel and Clinton Dattel at the Edgar Experimental Mine, who enabled and supported our fieldwork. We would also like to acknowledge the support of the two MLS instrumentation partners Mine Vision Systems which provided a Kaarta Stencil 2, and Emesent, which provided a Hovermap. We thank Scott Schiele, Pete Carney (Mine Vision Systems), and Stefan Hrabar (Emesent) for valuable discussions and technical advice.

Funding This work was funded by the National Institute of Occupational Safety and Health (NIOSH) under Grant Number 200-2016-90154.

Declarations

Conflict of Interest The authors declare no competing interests.

References

1. Kaiser PK, Cai M (2012) Design of rock support system under rockburst condition. J Rock Mechanics Geotech Eng. https://doi.org/10.3724/sp.j.1235.2012.00215
2. Mark C, Molinda GM (2004) "Preventing falls of ground in coal mines with exceptionally low-strength roof: two case studies," in 23rd Int Conference Ground Control Min, 2004
3. Nordlund E (2013) Deep hard rock mining and rock mechanics challenges. In Ground Supp 2013:39–56. https://doi.org/10.36487/ACG_rep/1304_02_Nordlund
4. Oraee K, Oraee N, Goodarzi A, Khajehpour P (2016) Effect of discontinuities characteristics on coal mine stability and sustainability: A rock fall prediction approach. Int J Min Sci Technol. https://doi.org/10.1016/j.ijmst.2015.11.012
5. Palei SK, Das SK (2008) Sensitivity analysis of support safety factor for predicting the effects of contributing parameters on roof falls in underground coal mines. Int J Coal Geol. https://doi.org/10.1016/j.coal.2008.05.004
6. Sandbak LA, Rai AR (2013) Ground support strategies at the turquoise ridge joint venture, Nevada. Rock Mech Rock Eng 46(3):437–454. https://doi.org/10.1007/s00603-012-0342-y
7. Fairhurst C (2017) Some Challenges of Deep Mining. Engineering 3(4):527–537. https://doi.org/10.1016/J.ENG.2017.04.017
8. Fahle L, Holley E, Walton G (2020) Toward a mine-wide, real-time, and autonomous geotechnical change detection, monitoring, and prediction framework for underground mines. In: Proceed 39th Int Conference Ground Control Min, ICGCM 2020
9. Dick GJ, Eberhardt E, Cabrejo-Liévano AG, Stead D, Rose ND (2015) Development of an early-warning time-of-failure analysis methodology for open-pit mine slopes utilizing ground-based slope stability radar monitoring data. Can Geotech J. https://doi.org/10.1139/cgj-2014-0028
10. Bonci G, Klappstein B, Maston W (2016) "Implementation of real time geotechnical monitoring at an open pit mountain coal mine in Western Canada (update)". In Landslides and Engineered Slopes. Exp Theory Practice 2:451–459
11. Benton DJ, Chambers AJ, Raffaldi MJ, Finley SA, Powers MJ (2016) Close-range photogrammetry in underground mining ground control. Remote Sens Syst Eng VI 9977:997707. https://doi.org/10.1117/12.2236691
12. Fekete S, Diederichs M, Lato M (2010) Geotechnical and operational applications for 3-dimensional laser scanning in drill and blast tunnels. Tunn Undergr Space Technol 25(5):614–628. https://doi.org/10.1016/j.tust.2010.04.008
13. Centers for Disease Control and Prevention (2021) "NIOSH Mine and Mine Worker Charts," 2021. https://wwwn.cdc.gov/niosh-mining/MMWC (accessed Sep. 03, 2021).
14 Jones E, Sofonia J, Canales C, Hrabar S, Kendoul F (2020) "Applications for the Hovermap autonomous drone system in underground mining operations. J South Afr Inst Min Metall 120(1):24–25. https://doi.org/10.17159/2411-9717/862/2020
15. Terzaghi K (1942) Shield tunnels of the Chicago Subway. J Boston Soc Civ Eng 29(3):163–210
16. Lu Y, Elsworth D, Wang L (2014) A dual-scale approach to model time-dependent deformation, creep and fracturing of brittle rocks. Comput Geotech 60:61–76. https://doi.org/10.1016/j.compgeo.2014.04.001
17. Walton G, Delaloye D, Diederichs MS (2014) Development of an elliptical fitting algorithm to improve change detection capabilities with applications for deformation monitoring in circular tunnels and shafts. Tunn Undergr Space Technol 43:336–349. https://doi.org/10.1016/j.tust.2014.05.014
18. Mercier-Langevin F, Hadjigeorgiou J (2011) Towards a better understanding of squeezing potential in hard rock mines. Min Technol 120(1):36–44. https://doi.org/10.1179/037178411X12942393517372
19. Mark C, Iannacchione AT (2000) Best Practices to mitigate injuries and fatalities from rock falls. In: Proceed 31st Ann Instit Min Health, Safe Res 115–129. https://stacks.cdc.gov/view/cdc/8586. Accessed 3 Sept 2021
20. Bitelli G, Dubbini M, Zanutta A (2004) Terrestrial laser scanning and digital photogrammetry techniques to monitor landslide bodies. Int Arch Photogramm, Remote Sens Spatial Inform Sci B5:246–251
21. Biasion A, Bornaz L, Rinaudo F (2005) Laser scanning applications on disaster management. In: Geo-information for Disaster Manage, Springer, 19–33. https://doi.org/10.1007/3-540-27468-5_2
22. Kromer RA, Abellán A, Hutchinson DJ, Lato M, Edwards T, Jaboyedoff M (2015) A 4D filtering and calibration technique for small-scale point cloud change detection with a terrestrial laser scanner. Remote Sens 7(10):13029–13058. https://doi.org/10.3390/rs71013029
23. Lato MJ, Jean Hutchinson D, Gauthier D, Edwards T, Ondercin M (2015) Comparison of airborne laser scanning, terrestrial laser scanning, and terrestrial photogrammetry for mapping differential slope change in mountainous terrain. Canadian Geotechnical J 52(2):129–140. https://doi.org/10.1139/cgj-2014-0051
24. Gigli G, Casagli N (2011) Semi-automatic extraction of rock mass structural data from high resolution LIDAR point clouds. Int J Rock Mech Min Sci 48(2):187–198. https://doi.org/10.1016/j.ijrmms.2010.11.009
25. Sturzenegger M, Stead D (2009) Quantifying discontinuity orientation and persistence on high mountain rock slopes and large landslides using terrestrial remote sensing techniques. Natural

Hazards Earth Syst Sci 9(2):267–287. https://doi.org/10.5194/nhess-9-267-2009
26. Sturzenegger M, Stead D (2009) Close-range terrestrial digital photogrammetry and terrestrial laser scanning for discontinuity characterization on rock cuts. Eng Geol 106(3–4):163–182. https://doi.org/10.1016/j.enggeo.2009.03.004
27. Abellán A, Jaboyedoff M, Oppikofer T, Vilaplana JM (2009) Detection of millimetric deformation using a terrestrial laser scanner: Experiment and application to a rockfall event. Natural Hazards Earth Syst Sci 9(2):365–372. https://doi.org/10.5194/nhess-9-365-2009
28. Oppikofer T, Jaboyedoff M, Blikra L, Derron MH, Metzger R (2009) Characterization and monitoring of the Åknes rockslide using terrestrial laser scanning. Natural Hazards Earth Syst Sci 9(3):1003–1019. https://doi.org/10.5194/nhess-9-1003-2009
29. Slob S, van Knapen B, Hack R, Turner K, Kemeny J (2005) Method for Automated Discontinuity Analysis of Rock Slopes with Three-Dimensional Laser Scanning. Transport Res Record: J Transport Res Board 1913(January):187–194. https://doi.org/10.3141/1913-18
30. Slob S, Hack HRGK, Feng Q, Röshoff K, Turner AK (2007) "Fracture mapping using 3D laser scanning techniques," 11th Congress of the International Society for Rock Mechanics, 299-302
31. Kemeny J, Turner K (2008) "Ground-based lidar: rock slope mapping and assessment," Lakewood, CO, Accessed: Jun. 14, 2022. [Online]. Available: https://rosap.ntl.bts.gov/view/dot/49768
32. Abellán A, Oppikofer T, Jaboyedoff M, Rosser NJ, Lim M, Lato MJ (2014) Terrestrial laser scanning of rock slope instabilities. Earth Surf Proc Land 39(1):80–97. https://doi.org/10.1002/esp.3493
33. Donovan J Ali WR (2008) "A change detection method for slope monitoring and identification of potential rockfall using three-dimensional imaging," 42nd U.S. Rock Mechanics - 2nd U.S.-Canada Rock Mechanics Symposium
34. Decker JB Dove JE (2008) "Laser scanning techniques in Devil's Slide tunnels," in Proceedings of the 42nd US rock mechanics symposium
35. Vöge M, Lato MJ, Diederichs MS (2013) Automated rockmass discontinuity mapping from 3-dimensional surface data. Eng Geol 164:155–162. https://doi.org/10.1016/j.enggeo.2013.07.008
36. Fekete S, Diederichs M (2013) Integration of three-dimensional laser scanning with discontinuum modelling for stability analysis of tunnels in blocky rockmasses. Int J Rock Mech Min Sci 57:11–23. https://doi.org/10.1016/j.ijrmms.2012.08.003
37. van Gosliga R, Lindenbergh R, Pfeifer N (2006) "Deformation analysis of a bored tunnel by means of terrestrial laser scanning," Proceedings of the ISPARS Commission V Symposium, 167–172
38. Delaloye D, Diederichs MS, Walton G, Hutchinson J (2014) Sensitivity Testing of the Newly Developed Elliptical Fitting Method for the Measurement of Convergence in Tunnels and Shafts. Rock Mech Rock Eng 48(2):651–667. https://doi.org/10.1007/s00603-014-0566-0
39. Walton G, Mills G, Fotopoulos G, Radovanovic R, Stancliffe RPW (2016) An approach for automated lithological classification of point clouds. Geosphere. https://doi.org/10.1130/GES01326.1
40. Walton G, Diederichs MS, Weinhardt K, Delaloye D, Lato MJ, Punkkinen A (2018) Change detection in drill and blast tunnels from point cloud data. Int J Rock Mech Min Sci 105(April):172–181. https://doi.org/10.1016/j.ijrmms.2018.03.004
41. Lemy F, Yong S, Schulz T (2009) "A case study of monitoring tunnel wall displacement using laser scanning technology," in Proceed 10th IAEG Congress' Eng Geol Tomorrow's cities', Nottingham 482
42. Nuttens T et al (2010) "High Resolution Terrestrial Laser Scanning for Tunnel Deformation Measurements," FIG Working Week 11–16, Accessed: Jun. 14, 2022. [Online]. Available: https://www.fig.net/resources/publications/prj/showpeerreviewpaper.asp?pubid=4497
43. Lindenbergh R, Uchanski L, Bucksch A, van Gosliga R (2009) Structural monitoring of tunnels using terrestrial laser scanning. In Rep Geodesy 2(87):231–239 (Available: http://resolver.tudelft.nl/uuid:0e58be05-ebe8-4345-9d06-9addc8c86470)
44. Karampinos E, Hadjigeorgiou J, Turcotte P, Mercier-Langevin F (2015) Large-scale deformation in underground hard-rock mines. J South Afr Inst Min Metall 115(7):645–652. https://doi.org/10.17159/2411-9717/2015/v115n7a11
45. Lato MJ, Diederichs MS (2014) Mapping shotcrete thickness using LiDAR and photogrammetry data: Correcting for over-calculation due to rockmass convergence. Tunn Undergr Space Technol 41(1):234–240. https://doi.org/10.1016/j.tust.2013.12.013
46. Slaker BA, Westman EC, Karfakis MG, Esterhuizen GS, Ripepi NS, Murphy MM (2015) Monitoring underground mine displacement using photogrammetry and laser scanning. Doctoral Dissertation, Virginia Polytechnic Institute and State University, Blacksburg
47. Slaker B, Murphy M, Winfield J (2019) Tracking convergence, spalling, and cutter roof formation at the pleasant gap limestone mine using LiDAR. 53rd U.S. Rock Mechanics/Geomechanics Symposium [Online]. Available: https://onepetro.org/ARMAUSRMS/proceedings-abstract/ARMA19/All-ARMA19/ARMA-2019-1566/124872)
48. Juneau L, Hurteau R, Freedman P, Chevrette G (1993) Using laser range data to model tunnel curvature for the automatic guidance of a mining vehicle. Proceed IEEE Conference Control Appl 2:643–648. https://doi.org/10.1109/cca.1993.348331
49. Thrunt S et al (2003) "A System for Volumetric Robotic Mapping of Abandoned Mines," in Proceedings of the 2003 IEEE International Conference on Robotics & Automation 4270–4275
50. Zlot R, Bosse M (2014) Three-dimensional mobile mapping of caves. J Cave Karst Stud 76(3):191–206. https://doi.org/10.4311/2012EX0287
51. Zlot R, Bosse M (2014) "Efficient Large-Scale 3D Mobile Mapping and Surface Reconstruction of an Underground Mine," in Field and Service Robotics: Results of the 8th International Conference, K. Yoshida and S. Tadokoro, Eds. Berlin, Heidelberg: Springer Berlin Heidelberg, 479–493. https://doi.org/10.1007/978-3-642-40686-7_32.
52. Zlot R, Bosse M (2014) Efficient large-scale 3D mobile mapping and surface reconstruction of an underground mine. Springer Tracts Adv Robotics 92:479–494. https://doi.org/10.1007/978-3-642-40686-7_32
53. Dewez TJB, Plat E, Degas M, Richard T, Pannet P, Al E (2016) "Handheld Mobile Laser Scanners Zeb-1 and Zeb-Revo to map an underground quarry and its above-ground surroundings," 2nd Virtual Geosciences Conference : VGC 2016, no. September, 1–4, [Online]. Available: https://www.researchgate.net/publication/308163385
54. Dewez TJB, Yart S, Thuon Y, Pannet P, Plat E (2017) Towards cavity-collapse hazard maps with Zeb-Revo handheld laser scanner point clouds. Photogramm Record 32(160):354–376. https://doi.org/10.1111/phor.12223
55. Eyre M, Wetherelt A, Coggan J (2016) Evaluation of automated underground mapping solutions for mining and civil engineering applications. J Appl Remote Sens. https://doi.org/10.1117/1.jrs.10.046011

56. Frangez V, Kramis B, Hübscher F, Baumann A (2018) Comparison of three innovative technologies for 3D-acquisition, modelling, and visualisation of an underground mine. In: FIG Congress 2018 [Online]. Available: https://www.fig.net/resources/proceedings/fig_proceedings/fig2018/papers/ts05c/TS05C_frangez_kramis_et_al_9502_abs.pdf
57. Hößelbarth D, Richter O, Martin C, Martienßen T, Wandinger M (2018) Comparison of three innovative technologies for 3D-acquisition, modelling, and visualization of an underground mine. In: FIG Congress 2018. [Online]. Available: https://www.oicrf.org/documents/40950/0/145_Paper_TS05C_frangez_kramis_et_al_9502.pdf/378c2177-c262-47c0-b5b7-2a2842df8ddc?t=1557397857912
58. Lavigne NJ, Marshall JA, Artan U (2010) "Towards underground mine drift mapping with RFID," Canadian Conference on Electrical and Computer Engineering, 1–6, https://doi.org/10.1109/CCECE.2010.5575165
59. Lynch BK, Marr J, Marshall JA, Greenspan M (2017) "Mobile LiDAR-based convergence detection in underground tunnel environments," Accessed: May 17, 2022. [Online]. Available: http://hdl.handle.net/1974/15638
60. Vanderbeck RL (2016) "A Bayesian Approach to Convergence Detection in Underground Excavations using LiDAR," Master's Thesis, Queen's University
61. Lavigne NJ, Marshall JA (2012) A Landmark-Bounded Method for Large-Scale Underground Mine Mapping. J Field Robotics 29(6):861–879. https://doi.org/10.1002/rob.21415
62. Juneau L, Hurteau R (1994) "Automatic guidance of a mining vehicle using laser range data: Simulation and preliminary experimental results," in Proc. 5th Int. Symp. on Robotics and Manufacturing 545–550
63. Scheding S et al (1997) Experiments in autonomous underground guidance. Proceed - IEEE Int Conference Robotics Automation 3:1898–1903. https://doi.org/10.1109/robot.1997.619065
64. Duff ES, Roberts JM, Corke PI (2003) Automation of an Underground Mining Vehicle using Reactive Navigation and Opportunistic Localization. IEEE Int Conference Intelligent Robots Syst 4(October):3775–3780. https://doi.org/10.1109/iros.2003.1249742
65. Roberts JM, Duff ES, Corke PI, Sikka P, Winstanley GJ, Cunningham J (2000) Autonomous control of underground mining vehicles using reactive navigation. Proceed-IEEE Int Conference Robotics Automation 4(April):3790–3795. https://doi.org/10.1109/ROBOT.2000.845322
66. Duff ES, Roberts JM (2006) Wall following with constrained active contours. Springer Tracts in Adv Robotics 24:51–60. https://doi.org/10.1007/10991459_6
67. Chadwick J (2000) Mine automation. Min Mag 183(1):12
68. Marshall JA, Larsson J (2008) Autonomous Underground Tramming for Center-Articulated Vehicles. J Field Robotics 25(6–7):400–421. https://doi.org/10.1002/rob.20242
69. Androulakis V, Sottile J, Schafrik S, Agioutantis Z (2021) Navigation system for a semi-autonomous shuttle car in room and pillar coal mines based on 2D LiDAR scanners. Tunn Undergr Space Technol 117:104149. https://doi.org/10.1016/j.tust.2021.104149
70. Thrun S (2004) Autonomous exploration and mapping of abandoned mines. IEEE Robot Autom Mag 11(4):79–91. https://doi.org/10.1109/MRA.2004.1371614
71. Baker C et al (2004) A campaign in autonomous mine mapping. Proceed - IEEE Int Conference on Robotics Automation 2004(2):2004–2009. https://doi.org/10.1109/robot.2004.1308118
72. Silver D, Carsten J, Thayer S (2006) Topological global localization for subterranean voids. Springer Tracts in Adv Robotics 25:117–128. https://doi.org/10.1007/978-3-540-33453-8_11
73. Fairfield N, Wettergreen D (2009) "Evidence grid-based methods for 3D map matching," Proceedings - IEEE Int Conference Robotics Automation, 1637–1642, https://doi.org/10.1109/ROBOT.2009.5152688
74. Morris A et al (2005) Recent Developments in Subterranean Robotics. J Field Robotics 23(1):35–57. https://doi.org/10.1002/rob
75. Lajoie PY, Ramtoula B, Chang Y, Carlone L, Beltrame G (2020) DOOR-SLAM: Distributed, Online, and Outlier Resilient SLAM for Robotic Teams. IEEE Robotics Automation Lett 5(2):1656–1663. https://doi.org/10.1109/LRA.2020.2967681
76. Kramer A, Kasper M, Heckman C (2019) "VI-SLAM for Subterranean Environments," Field and Service Robotics (FSR), pp. 1–15
77. Ebadi K et al (2020) "LAMP: Large-Scale Autonomous Mapping and Positioning for Exploration of Perceptually-Degraded Subterranean Environments
78. Miller ID et al (2019) Mine Tunnel Exploration using Multiple Quadrupedal Robots. IEEE Robotics Automation Lett 5(2):2840–2847 (Available: http://arxiv.org/abs/1909.09662)
79. Nüchter A, Surmann H, Lingemann K, Hertzberg J, Thrun S (2004) 6D SLAM with an application in autonomous mine mapping. Proceed - IEEE Int Conference Robotics Automation 2004(2):1998–2003. https://doi.org/10.1109/robot.2004.1308117
80. Bosse M, Zlot R (2009) "Continuous 3D scan-matching with a spinning 2D laser," in IEEE Int Conference Robotics Automation 4312–4319. https://doi.org/10.1109/robot.2009.5152851
81. Hößelbarth D, Richter O, Martin C, Martienßen T, Wandinger M (2018) "Erste Erfahrungen mit dem handgeführten Laserscanner ZEB-REVO bei Vermessungsarbeiten im Altbergbau am Südtiroler Schneeberg Das Bergwerk am Schneeberg in Südtirol – über 800 Jahre Bergbaugeschichte," 1–14
82. Andrews P, Rwodzi L, Ekkerd J, Ratshitaka N (2019) Advanced techniques for the monitoring of pillar and excavation behaviour at a deep level massive mine. Proceed Ninth Int Conference Deep High Stress Min June:133–148. https://doi.org/10.36487/acg_rep/1952_11_andrews
83. Jones E, Ghabraie B, Beck D (2018) "A method for determining field accuracy of mobile scanning devices for geomechanics applications", ISRM International Symposium - 10th Asian Rock Mechanics Symposium. ARMS 2018:978–981
84. Turner RM, Bhagwat NP, Galayda LJ, Knoll CS, Russell EA, MacLaughlin MM (2018) Geotechnical characterization of underground mine excavations from UAV-captured photogrammetric & thermal imagery. 52nd U.S. Rock Mechanics/Geomechanics Symposium. [Online] Available: https://onepetro.org/ARMAUSRMS/proceedings-abstract/ARMA18/All-ARMA18/ARMA-2018-508/122614
85. Turner RM, MacLaughlin MM, Iverson SR (2020) Identifying and mapping potentially adverse discontinuities in underground excavations using thermal and multispectral UAV imagery. Eng Geol 266:105470. https://doi.org/10.1016/j.enggeo.2019.105470
86. Emesent, "Hovermap," (2021) https://www.emesent.com/hovermap/
87. Kaarta, "Kaarta Products,"(2022) https://www.kaarta.com/products/stencil-2-for-rapid-long-range-mobile-mapping/
88. Park C, Moghadam P, Kim S, Elfes A, Fookes C, Sridharan S (2018) Elastic LiDAR Fusion: Dense Map-Centric Continuous-Time SLAM. Proceed - IEEE Int Conference Robotics Automation. https://doi.org/10.1109/ICRA.2018.8462915
89. Zhang J, Singh S (2015) Visual-lidar odometry and mapping: Low-drift, robust, and fast. Proceed - IEEE Int Conference Robotics Automation June:2174–2181. https://doi.org/10.1109/ICRA.2015.7139486
90. Sofonia JJ, Phinn S, Roelfsema C, Kendoul F, Rist Y (2019) Modelling the effects of fundamental UAV flight parameters

on LiDAR point clouds to facilitate objectives-based planning. ISPRS J Photogramm Remote Sens 149(January):105–118. https://doi.org/10.1016/j.isprsjprs.2019.01.020
91. Soudarissanane S, Lindenbergh R, Menenti M, Teunissen P (2011) Scanning geometry: Influencing factor on the quality of terrestrial laser scanning points. ISPRS J Photogramm Remote Sens 66(4):389–399. https://doi.org/10.1016/j.isprsjprs.2011.01.005
92. Toschi I, Rodríguez-Gonzálvez P, Remondino F, Minto S, Orlandini S, Fuller A (2015) "Accuracy evaluation of a mobile mapping system with advanced statistical methods", International Archives of the Photogrammetry. Remote Sens Spatial Informa Sci - ISPRS Arch. https://doi.org/10.5194/isprsarchives-XL-5-W4-245-2015
93. International Organization for Standardization, "ISO 5725," (2021) https://www.iso.org/obp/ui/#iso:std:iso:5725:-1:en
94. Velodyne LiDAR (2022) "Velodyne LiDAR 'Puck' LITE Light Weight Real-Time 3D LiDAR Sensor: Product Specification". https://velodynelidar.com/products/puck-lite/
95. Zhang J, Singh S (2017) Low-drift and real-time lidar odometry and mapping. Auton Robot 41(2):401–416. https://doi.org/10.1007/s10514-016-9548-2
96. CSIRO (2022) "Wildcat SLAM – our next-generation 3D SLAM Software," https://data61.csiro.au/en/Our-Research/Our-Work/Monitoring-the-Environment/Visualising-the-world/Wildcat-SLAM
97. FARO (2019) "FARO FOCUS LASER SCANNERS - Features," https://www.faro.com/products/construction-bim/faro-focus/features/No Title
98. FARO (2015) "FARO ® Laser Scanner Focus 3D X 330 The Perfect Instrument for 3D Documentation FARO ® Laser Scanner Focus 3D X 330," 3–4
99. CloudCompare (2021) "CloudCompare," https://www.danielgm.net/cc/
100. Maptek (2021) "PointStudio."
101. Lague D, Brodu N, Leroux J (2013) Accurate 3D comparison of complex topography with terrestrial laser scanner: Application to the Rangitikei canyon (N-Z). ISPRS J Photogramm Remote Sens. https://doi.org/10.1016/j.isprsjprs.2013.04.009
102. RStudio PBC, "R Studio." RStudio, PBC, Boston, 2021. [Online]. Available: https://www.rstudio.com/
103. Fekete S, Diederichs M, Lato M (2010) Geotechnical and operational applications for 3-dimensional laser scanning in drill and blast tunnels. Tunn Undergr Space Technol 25(5):614–628. https://doi.org/10.1016/j.tust.2010.04.008
104. Gallwey J, Eyre M, Coggan J (2021) "A machine learning approach for the detection of supporting rock bolts from laser scan data in an underground mine," Tunnelling and Underground Space Technology, 107 https://doi.org/10.1016/j.tust.2020.103656
105. Watson C, Marshall J (2018) Estimating underground mine ventilation friction factors from low density 3D data acquired by a moving LiDAR. Int J Min Sci Technol 28(4):657–662. https://doi.org/10.1016/j.ijmst.2018.03.009
106. Engin IC, Maerz NH, Boyko KJ, Reals R (2020) Practical Measurement of Size Distribution of Blasted Rocks Using LiDAR Scan Data. Rock Mech Rock Eng 53(10):4653–4671. https://doi.org/10.1007/s00603-020-02181-5
107. Zhang J, Singh S (2018) Laser–visual–inertial odometry and mapping with high robustness and low drift. J Field Robotics 35(8):1242–1264. https://doi.org/10.1002/rob.21809
108. E. Jones and D. Beck (2018) "The use of three-dimensional laser scanning for deformation monitoring in underground mines," 13th AusIMM Underground Operators' Conference, 1–7
109. Singh SK, Banerjee BP, Raval S (2021) "Three dimensional unique identifier based automated georeferencing and coregistration of point clouds in underground environment," Remote Sensing, 13, no. February https://doi.org/10.3390/rs13163145
110. Evans P (2021) "Improving Convergence Monitoring Using Lidar Data At Rio Tinto ' S Argyle Diamond Mine Improving Convergence Monitoring Using Lidar Data At Rio Tinto ' S Argyle Diamond Mine." pp. 1–12, [Online]. Available: https://www.emesent.io/2021/05/26/improving-convergence-monitoring-using-lidar-data-at-rio-tintos-argyle-diamond-mine/
111. DiFrancesco PM, Bonneau D, Hutchinson DJ (2020) "The implications of M3C2 projection diameter on 3D semi-automated rockfall extraction from sequential terrestrial laser scanning point clouds," Remote Sensing, 12, 11 https://doi.org/10.3390/rs12111885
112. Iannacchione A et al (2020) Evaluation of stress-control layout at the Subtropolis Mine, Petersburg, Ohio. Int J Min Sci Technol 30(1):77–83. https://doi.org/10.1016/j.ijmst.2019.12.009